# ANALYSIS AND USE OF VAS SATELLITE DATA

Final Report

Grant NAG8-033

by

Henry E. Fuelberg
Principal Investigator

and

Mark J. Andrews
John L. Beven II
Steven R. Moore
Bradley M. Muller

Department of Meteorology
The Florida State University
Tallahassee, Florida 32306

August 23, 1985--August 22, 1988

# ANALYSIS AND USE OF VAS SATELLITE DATA

Final Report

Grant NAG8-033

by

Henry E. Fuelberg
Principal Investigator

and

Mark J. Andrews
John L. Beven II
Steven R. Moore
Bradley M. Muller

Department of Meteorology
The Florida State University
Tallahassee, Florida 32306

August 23, 1985--August 22, 1988

# ABSTRACT

Four interrelated investigations have examined the analysis and use of VAS satellite data. A case study of VAS-derived mesoscale stability parameters suggested that they would have been a useful supplement to conventional data in the forecasting of thunderstorms on the day of interest. However, the meteorological significance of small or short lived stability features was uncertain.

A second investigation examined the roles of first guess and VAS radiometric data in producing sounding retrievals. It appeared that the radiance data often did not have a decisive influence on the final satellite soundings for this case. Broad-scale patterns of the first guess, radiances, and retrievals frequently were similar, whereas small scale retrieval features, especially in the dew points, were often of uncertain origin.

Two research tasks considered 6.7 micron middle tropospheric water vapor imagery. The first utilized radiosonde data to examine causes for two areas of warm brightness temperature. Subsidence associated with a translating jet streak was important in producing one image streak, while the second was related to a tropopause fold, i.e., a downward extrusion of dry stratospheric air into the middle troposphere.

The second task involving water vapor imagery investigated simulated imagery created from LAMPS output and a radiative transfer algorithm. Simulated image patterns were found to compare favorably with those actually observed by VAS. Furthermore, the mass/momentum fields from LAMPS were a powerful tool for understanding causes for the image configurations. Model trajectory calculations were especially useful in this regard.

TABLE OF CONTENTS

# LIST OF TABLES

# LIST OF FIGURES

# ANALYSIS AND USE OF VAS SATELLITE DATA

## I. INTRODUCTION

The geostationary platform was a major advance in meteorological satellite technology. The original geostationary satellites contained only visible and infrared window channels; however, in November 1980, GOES-4 was launched with a new Visible-Infrared Spin-Scan Radiometer (VISSR). This new instrument, called the VISSR Atmospheric Sounder (VAS), has imaging capabilities in numerous spectral channels, thereby permitting sounding estimates to be made from geostationary orbit for the first time. Because of its greatly improved data collection frequency in comparison to the polar orbiters, the GOES/VAS system was expected to be an important aid in the diagnosis and forecasting of subsynoptic-scale phenomena such as severe thunderstorms.

A major goal of today's satellites is to provide radiance data from which vertical soundings of temperature and humidity can be obtained. Unfortunately, however, this is not a trivial task. The radiative transfer equations which govern the retrieval process are complex, and the solutions are not unique. One of the emphases of our research was to investigate the relative importance of first guess numerically-derived sounding profiles and radiometric channel data in producing VAS retrievals. Another effort explored the use of VAS retrievals toward understanding the thermodynamic processes which led to the severe thunderstorms on 21 July 1982.

The recent literature also suggests that values, gradients, and patterns in the radiance images themselves have direct synoptic applications. In this regard, the grant considered 6.7 micron middle tropospheric water vapor imagery on 6-7 March 1982, one of the days of the VAS Demonstration Experiment. Pronounced bands of warm brightness temperature occurred during this period. One of the studies employed radiosonde data to explore the dynamic processes associated with the image streaks. A second study of the same period utilized output from a mesoscale model simulation to further understand factors leading to the image patterns.

Each of the four above mentioned components of the grant activities constituted the thesis research for a graduate student at Florida State University. Abridged versions of

1

each thesis comprise a chapter in the current final report. In addition, each of the activities has been reported at conferences sponsored by the American Meteorological Society in early 1988. Copies of any of these conference papers or theses are available by contacting Prof. Fuelberg.

II.  ASSESSMENT OF VAS-DERIVED PRODUCTS CREATED BY A

SIMULTANEOUS ALGORITHM ON A CONVECTIVELY ACTIVE DAY


A.  Introduction


The National Severe Storms Forecast Center currently
receives VAS retrievals prepared from a physical algorithm,
i.e., an inversion of the radiative transfer equation (Hayden,
1988).  Their operational use has been described by Anthony
and Wade (1983) and Mosher and Schoeni (1988).  This aspect of
the grant research examined VAS-derived stability parameters
for a case of severe thunderstorms in July 1982.  The primary
emphasis was whether VAS provided information not available
from radiosondes or surface reports.  Details of the research
are given in Andrews (1987) and Andrews and Fuelberg (1988)
while highlights are presented here.


B.  Data and Weather Conditions


VAS retrievals were available at 1300, 1600, 1700, 2000
and 2300 GMT 21 July 1982, having been prepared at the
University of Wisconsin-Madison.  National Meteorological
Center 12 h forecasts were first guess profiles for the 1300
GMT retrievals, but previous VAS profiles were employed
thereafter.  Soundings were edited to eliminate profiles
contaminated by clouds or inconsistent with surrounding data.
The final data set consisted of retrievals at an approximate
spacing of 125 km with few major gaps due to cloud cover.

The synoptic situation for 21 July 1982 has been
described in detail by Fuelberg and Funk (1987).  Briefly
stated, however, the surface chart at 1200 GMT (Fig. 1)
depicted a weak stationary front extending from a low pressure
area over Colorado through Missouri and northern Georgia.  A
cold front stretched from Wisconsin to Nebraska and Montana.
Conditions at 850 mb (Fig. 1) included high pressure and
abundant moisture over the middle Mississippi River Valley.
At 500 mb (Fig. 1), a weak trough was over the Midwest States

3
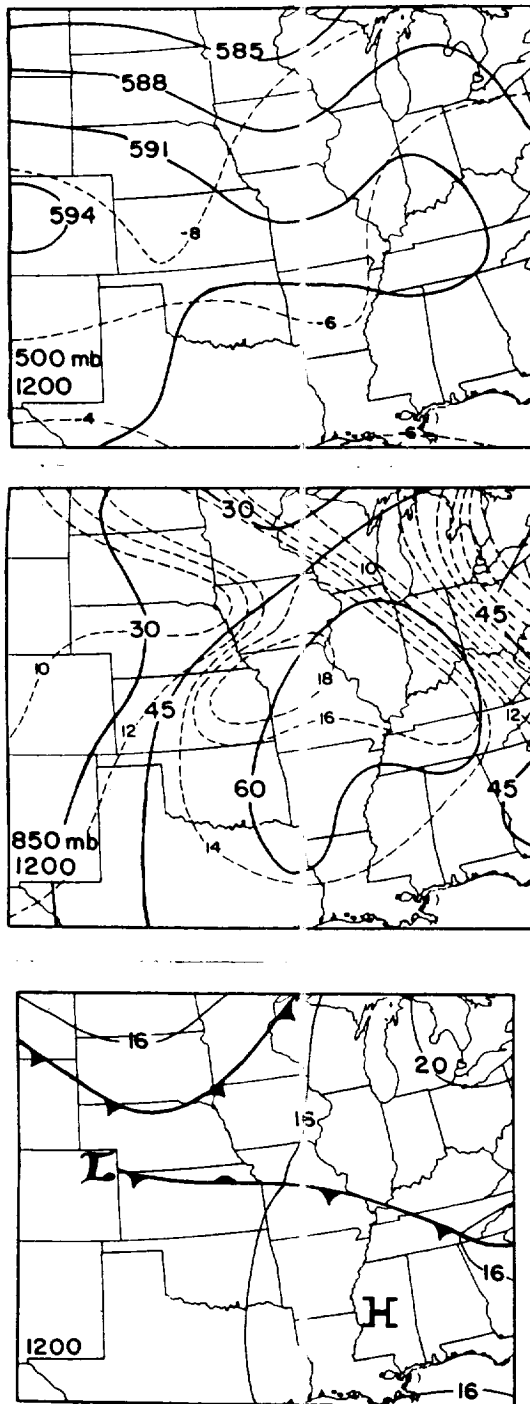
Fig. 1. Analyses at 1200 GMT 21 July 1982 and NMC radar summaries at 2335 GMT. At the surface, isobars are in the usual convention. At 850 mb, heights are solid where 45 denotes 1450 m, and isodrosotherms (dashed) are in $^{\circ}$C. At 500 mb, heights (solid) are in decameters and temperatures (dashed) are in $^{\circ}$C. Echo tops are in km.

4
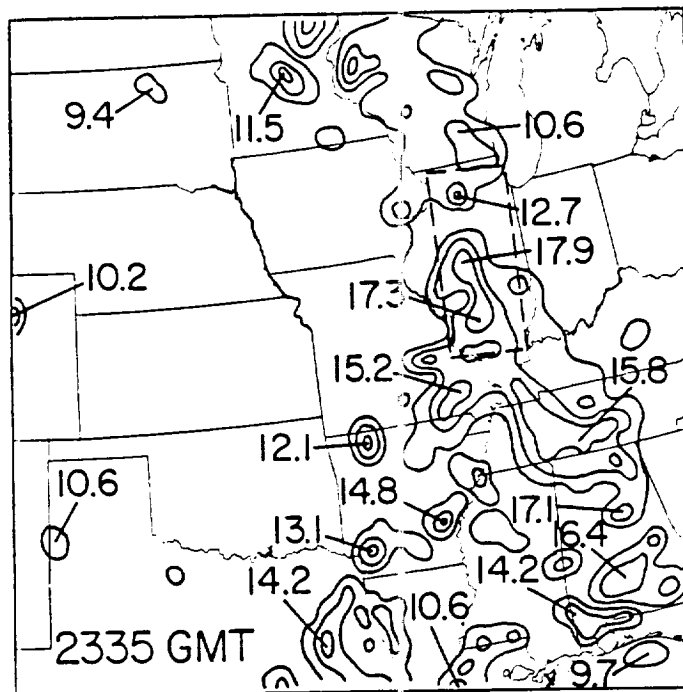
Fig. 1. (Continued)

while ridging extended ahead and into a major high over Colorado. Jet stream activity was along the Great Lakes.

Early morning radiosonde-derived Lifted Indices (LI) indicated relatively unstable air from Kansas to Illinois to the Gulf Coast. Thus, only a "triggering" mechanism was needed to initiate convection. Fuelberg and Funk (1987), who calculated large scale vertical motions from VAS retrievals, found ascent eastward of the 500 mb trough. They also noted surface moisture convergence in the vicinity of the stationary front and several outflow boundaries that were remnants of the previous night's convection.

The convection of special interest to this study developed over western Kentucky, central Arkansas, and southern Illinois near 1800 GMT 21 July. Radar summaries (Fig. 1) indicate tops exceeding 17 km later during the afternoon.

## C. Lifted Index Patterns

Five panels of VAS-derived LI are given in Fig. 2 along with the sonde-derived version at 0000 GMT 22 July. Each is a subjective analysis of values at the individual sounding sites. The relative minimum (-6) over eastern Missouri at 1300 GMT becomes as stable as -3 during the day. Since the surroundings become much more unstable between 2000-2300 GMT, the area then appears relatively stable. This comparative afternoon stability may result from early morning convection west of the area. Specifically, a strong eastward moving outflow boundary is evident in satellite imagery and surface reports (not shown). VAS retrievals east and west of the boundary at 2000 GMT (marked by ●'s in Fig. 2) are shown in Fig. 3a. The drier downdraft air to the west appears to limit storm development since there is no convection over central Missouri after 1700 GMT.

Another feature at 1300 GMT (Fig. 2) is the relative instability (-6) over northern Mississippi. It seems to migrate northward during the day, reaching -8 at 1700 GMT and -10 by 2000 GMT before diminishing at 2300 GMT due to the storms over Illinois, the most intense convection of the period. To explore the evolving stability, VAS-derived soundings for 1300 and 2000 GMT over southern Illinois (X at 1300 and ● at 2000 GMT in Fig. 2) are given in Fig. 3b. The morning profile exhibits a common severe weather configuration, i.e., a shallow moist layer near the surface capped by an inversion and drier air aloft. In the afternoon

6
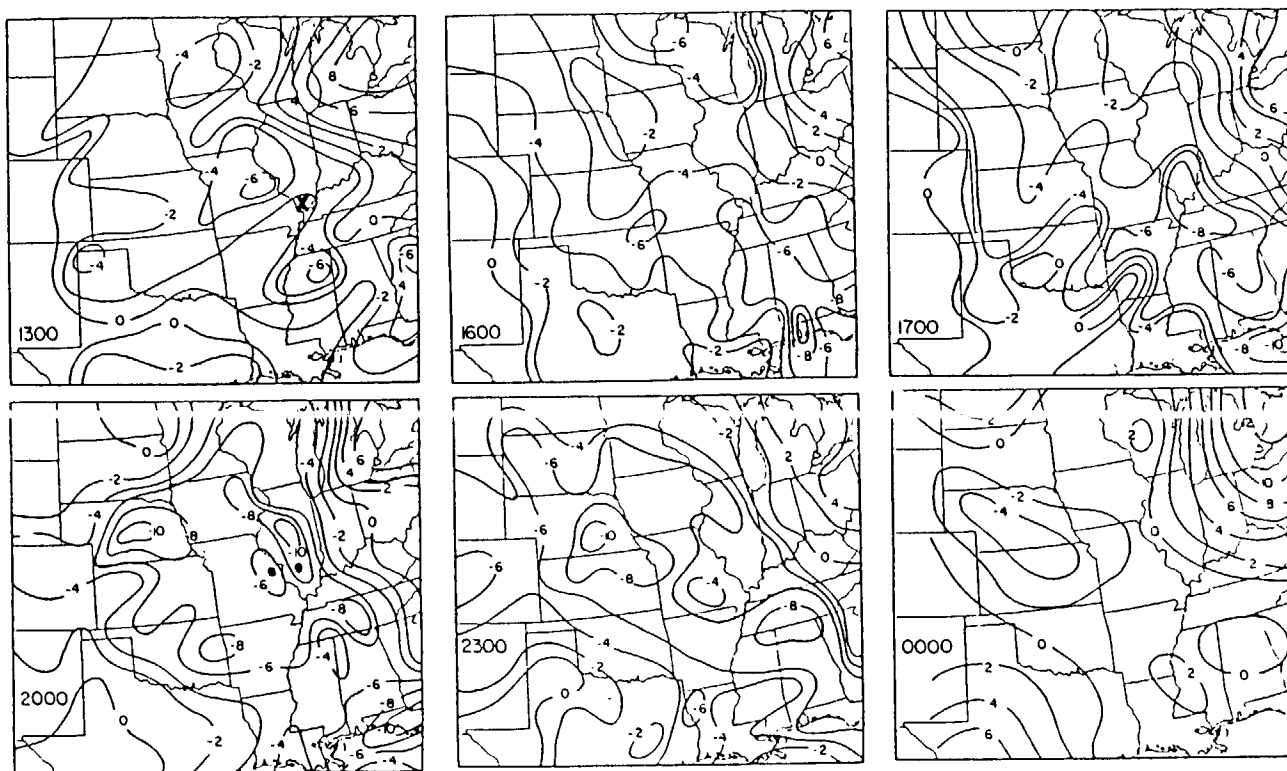
Fig. 2. VAS-derived LI between 1300-2300 GMT 21 July, and
sonde-derived LI at 0000 GMT 22 July.
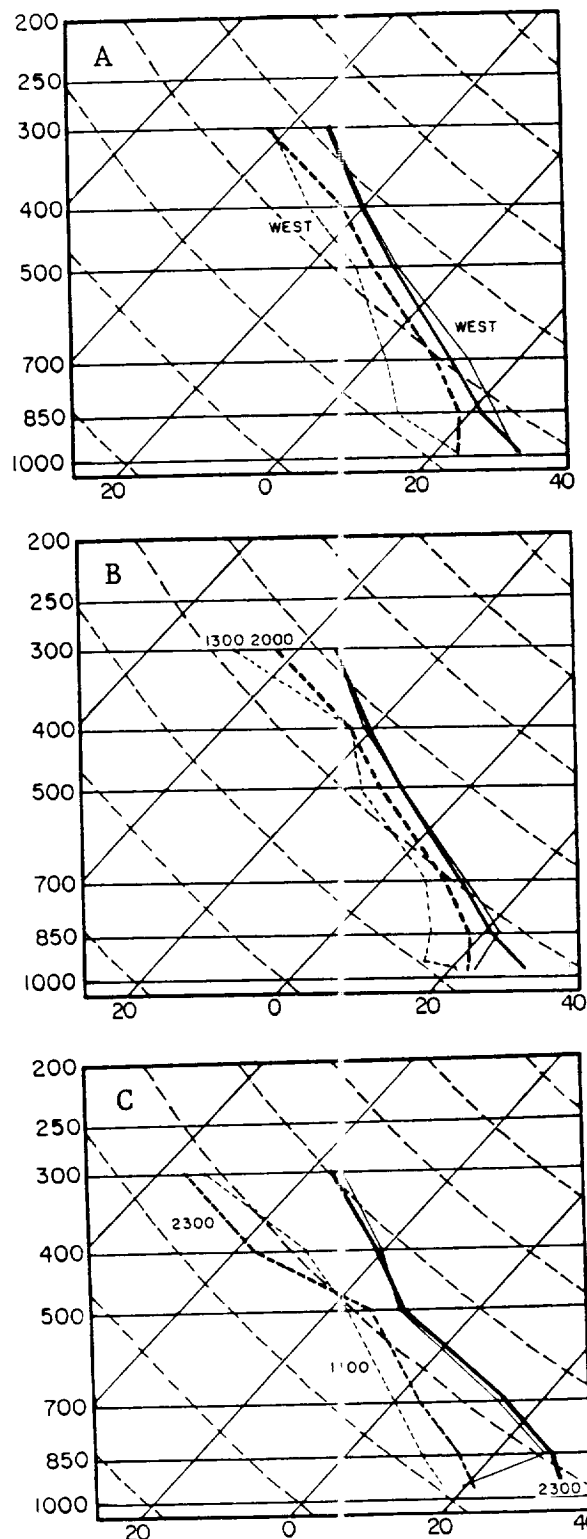
Fig. 3. Skew T-log p diagrams of VAS soundings. A contrasts conditions east (heavy) and west (thin) of an outflow boundary at 2000 GMT. B contrasts conditions over southern Illinois between 1300 (thin) and 2000 GMT (heavy). C contrasts conditions over Nebraska between 1300 (thin) and 2300 GMT (heavy). Sounding locations are given in Fig. 2.

sounding, surface heating has destroyed the morning inversion while moisture has increased at all levels. With the exception of the boundary layer, temperatures are relatively static.

The convection over southern Alabama and the Florida panhandle (Fig. 1) occurs near another LI minimum, -6 over Georgia at 1300 GMT (Fig. 2). The region shifts slowly southwestward while exhibiting increasing instability (-10). On the other hand, there is an axis of relatively stable air from Louisiana to southern Mississippi at all five VAS times, and satellite imagery indicates little convection in that area during the entire day.

The final area of interest is major instability (-10) that is first evident over Nebraska at 2000 GMT (Fig. 2) and is later confirmed by sonde reports at 0000 GMT (Fig. 2). This originally appeared to be a "false alarm"; however, strong convection did develop during the upcoming evening, eventually forming a Mesoscale Convective Complex (MCC) over northeastern Kansas. Examination of nearby 1300 and 2300 GMT VAS profiles (Fig. 3c) reveals marked low level warming and increasing low to mid level moisture. VAS exaggerates the morning inversion, but there is a nearly dry adiabatic lapse rate between 850 and 500 mb at both times.

There is one notable area where VAS-derived LI (Fig. 2) is not a good indicator of convective activity. Although showers and thunderstorms develop over extreme eastern Texas during the afternoon (Fig. 1), LI remains in the relatively stable 0 to -2 range. Morning skies are cloud free, providing abundant solar heating, and apparently there is sufficient small scale forcing to "trigger" even this region.

In summary, except for eastern Texas, the most unstable regions coincide with convection, while more stable areas are storm free. On the other hand, a comparison of VAS- and sonde-derived values near 0000 GMT (Fig. 2) and 1200 GMT (not shown) indicates that the satellite versions are too negative, an aspect noted by Anthony and Wade (1983) and others. Thus, a forecaster must concentrate on relative magnitudes and evolutions of patterns, and not specific values. In a related fashion, the meteorological significance that should be ascribed to small scale LI features remains to be determined. Fuelberg and Meyer (1986) performed error analyses of VAS physical retrievals (temperature and humidity) which suggests an LI uncertainty of several units. In general, the larger and more persistent LI variations are most likely to be significant; however, we are investigating this aspect in greater detail.

An important question remains: Did VAS-derived LI variations result simply from information available from conventional surface reports? That is, was VAS merely providing information that could have been computed, for

9

example, from the Hales and Doswell (1982) procedure which
utilizes assumed 500 mb temperatures together with hourly
surface data?  To investigate, we recalculated the LIs at 1600
and 2000 GMT using their procedure, one that is commonly
employed at the National Severe Storms Forecast Center.  The
major assumption is that the surface is representative of the
entire 1 km boundary layer.  Since sonde-derived 500 mb
temperatures varied less than $2^{\circ}C$ between 1200-0000 GMT, we
assumed no change over the 4 h period between 1600-2000 GMT.
Once  the surface-derived indices were calculated at the two
individual times, they were subtracted to yield LI changes
solely attributable to varying surface conditions (Fig. 4a).
Corresponding LI changes from the VAS retrievals are shown in
Fig. 4b (individual times are in Fig. 2).

If VAS were providing no additional information than the
surface reports, the two LI change fields would be similar
(Figs. 4a, b).  Although that is the case over much of
Nebraska, the LI changes generally are quite dissimilar.  Over
the Illinois-Iowa border, for example, VAS-derived LI
decreases more rapidly with time than the surface-derived
version.  Conversely, there are opposite situations as well.
As to the cause for these differences, the VAS LIs are based
on a time varying 500 mb temperature, not the constant value
assumed in Fig. 4a, and the vapor content of the lowest
kilometer, not just the surface.  Of these two factors, we
found the low level vertical distribution of water vapor to be
most important.  Thus, it should not necessarily be assumed
uniform, a point previously noted by Mostek et al. (1986).


D.   Integrated Stability Parameters


Since the various VAS channels sense radiation over deep
atmospheric layers, stability indices based on layer data
might be more appropriate than those derived from a few
discrete levels.  Utilizing the procedures of Zehr et al.
(1988), we calculated several types of positive and negative
energy parameters.

Fields of VAS-derived positive buoyant energy (PBE, not
shown) were similar to those of LI (Fig. 2) since procedures
for obtaining them are closely related.  Specifically, the LI
is the difference between the lifted parcel temperature and
the 500 mb environmental value, while PBE is the integrated
temperature difference between the raised parcel and the
environmental sounding at all altitudes above the Level of
Free Convection (LFC).  Since VAS data only are available at
the mandatory levels and have relatively few vertical
features, the 500 mb value has a major impact on the overall
sounding.

A



B
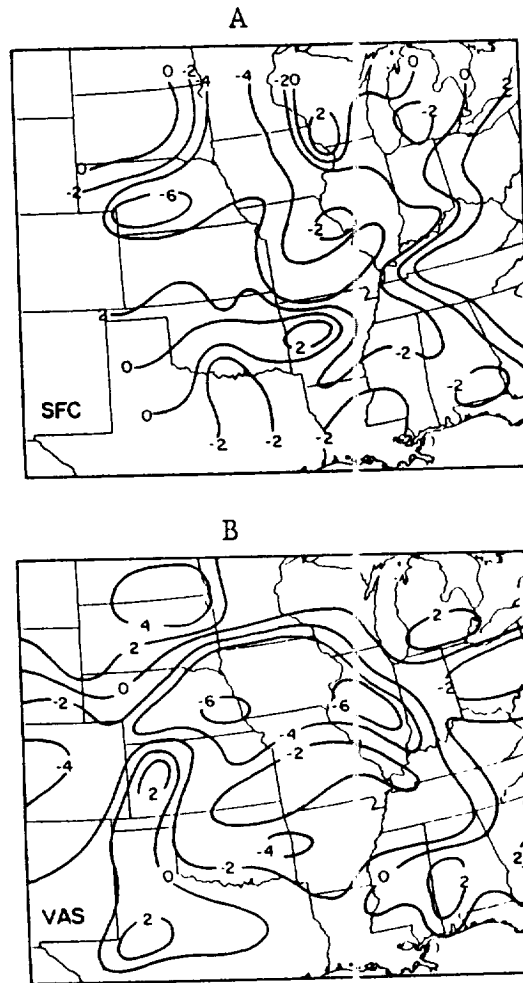


Fig. 4. A: Differences in surface-derived LI between 1600-2000 GMT. B: Differences in VAS-derived LI between 1600-2000 GMT.

Negative energy (NE) describes the hurdle which a parcel must overcome before even large PBE can be utilized. Values of VAS-derived NE in Fig. 5 are the sum of negative values between the surface and LFC. In general, NE maxima correspond to little convection, regardless of PBE strength, and rarely does deep convection occur with NE greater than 250 J/kg. Of special interest is the evolution of values near Nebraska. NE is approximately 600 J/kg between 1300-1700 GMT, but there is a 40-50% decrease thereafter. This trend of decreasing suppression, if continued, could account for the fact that convection in the area does not begin until approximately 0600 GMT in spite of low LI (Fig. 2) and large PBE. One should also note the axis of relatively small NE over the Mississippi River Valley.


E.    Conclusions


VAS-derived stability parameters are routinely available to forecasters at the Severe Storms Forecast Center. This case study suggests that they would have been a useful supplement to conventional data on 21 July 1982. Patterns and evolutions of LI frequently were associated with either the development or lack of convection, and the LI variations were not simply attributable to changes in surface conditions. NE patterns appeared to describe processes inhibiting convective initiation. Of course, adequate water vapor and a lifting mechanism must accompany instability before convection can begin.

The 2-3 h frequency and 100-150 km spacing of VAS retrievals are superior to those of any other operational data source. Yet, the meteorological significance of small scale VAS-derived stability fluctuations is still uncertain. For example, cloud contamination and limitations of the sensor and/or retrieval algorithm can lead to unrepresentative retrievals and stability data. These limitations of VAS products must be understood and handled before forecasters can use the data effectively.
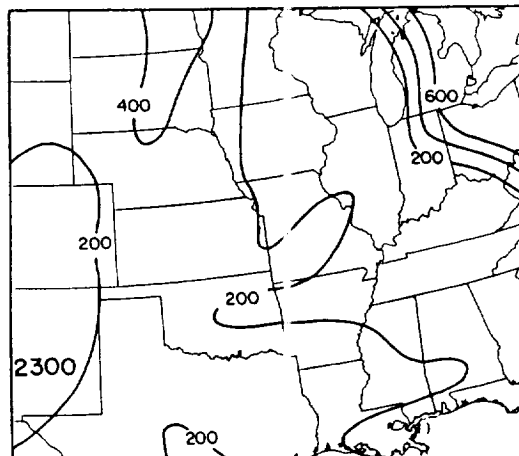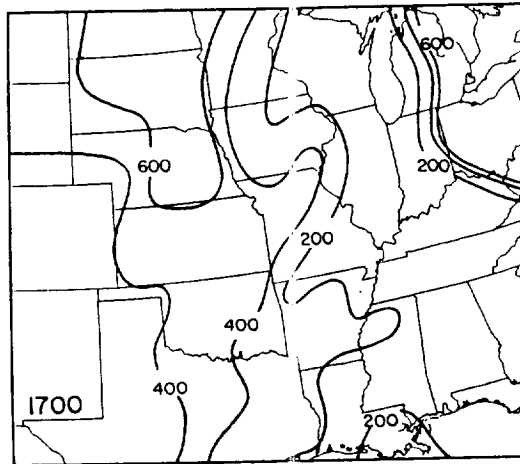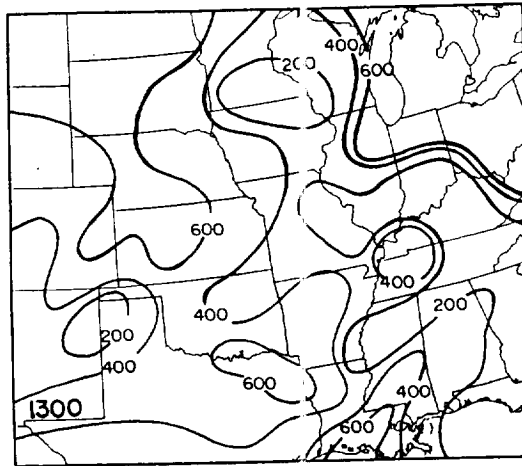
Fig. 5.  VAS-derived NE (J/kg) at selected times between 1300-
2300 GMT 21 July.

13

# III.  RELATIONS BETWEEN VAS SOUNDINGS AND

# THEIR FIRST GUESS INPUT

## A.  Introduction

VAS senses radiation in the visible band plus 12 channels of the infrared spectrum.  Two algorithms have been used operationally to retrieve vertical profiles of temperature and dewpoint from VAS radiances.  Both are physical procedures in which the radiative transfer equation is inverted (Smith, 1983; Hayden, 1988).  Since the retrieval solution is not unique, a "first guess" sounding must be provided as input. The Smith (1983) version employs an iterative technique to compute the profiles of temperature and humidity, and after obtaining initial values, an analytical least squares procedure enhances their vertical structure.

Since the physical retrieval algorithm requires both satellite radiances and a first guess profile, the question arises, "How much does the final retrieved sounding depend on each of these two inputs?"  This aspect of the grant research attempted to answer that question for the Smith (1983) algorithm.  The study employed 1) Comparisons between radiosonde, VAS, and first guess profiles to determine whether the VAS soundings were more accurate than the first guesses when compared to the sonde-measured ground truth, and 2) Statistical structure and correlation function analyses of VAS, first guess, and brightness temperature data to determine which of the two inputs was providing the most information to the final retrieved soundings.  Details of the research are provided in Beven (1988) and Beven and Fuelberg (1988) while highlights are presented here.

## B.  Data and Methodology

The use of structure and correlation functions on a time series of data at single sites was described by Gandin (1963). The modification used in this study permitting the analysis of a data field at individual times was developed by Hillger and Vonder Haar (1979) and employed by Fuelberg and Meyer (1986).

Four types of data were used in the study of 6-7 March 1982, one of the days of the VAS Demonstration Experiment. VAS soundings of temperature and dew point over the southcentral United States were available at seven times. They were created at the University of Wisconsin-Madison and were at spacings of 75-100 km over cloud free areas. They are identical to the retrievals employed by Jedlovec (1985) and Fuelberg and Meyer (1986). The second data type was the first guess (FG) profiles used to create the retrievals. They were based on time interpolation of 12 h output from the Limited Fine Mesh (LFM) model. Twelve channels of VAS brightness temperatures (TBs) constituted the third data type. Finally, rawinsonde (RAOB) profiles from National Weather Service sites and a special network served as ground truth.

A series of steps was used to prepare the TBs for subsequent use. First, garbled or missing scan lines were removed, and the originally oversampled scan lines were averaged to yield fields of view that were approximately 16 x 14 km. Then, all detectable cloudy views were removed from the data set, and a correction for varying satellite zenith angle was applied. Finally, the 16 x 14 km pixels were further averaged over 5 x 5 arrays in order to simulate how the data were used in the retrieval algorithm. This was done relative to the FG/VAS sites, with the center of each 5 x 5 array being as close as possible to the retrieval site.

Processing of the VAS retrievals and FG data involved the removal of soundings not located in the clear sky region of the radiance data. This was necessary because our cloud detection criteria were more stringent than those used during the original preparation of retrievals. The only processing of the sonde data was a time adjustment to account for non-simultaneous release.

## C.  Pairing Results

The first aspect of this research was a simple level-by-level comparison between the RAOB data and nearby VAS/FG profiles. Specifically, each RAOB site was paired with the nearest VAS retrieval within 100 km, with consideration of sonde drift being included. This procedure permitted the statistical evaluation of the retrievals against their FG input and the "ground truth" sonde data.

Results from pairing the radiosonde sites with nearby VAS retrievals are given in Fig. 6. Values at most levels are based on at least 90 pairings and represent the composite of the 7 observation times. The lack of sonde-derived humidity above 400 mb prevented calculations in the upper troposphere.

15
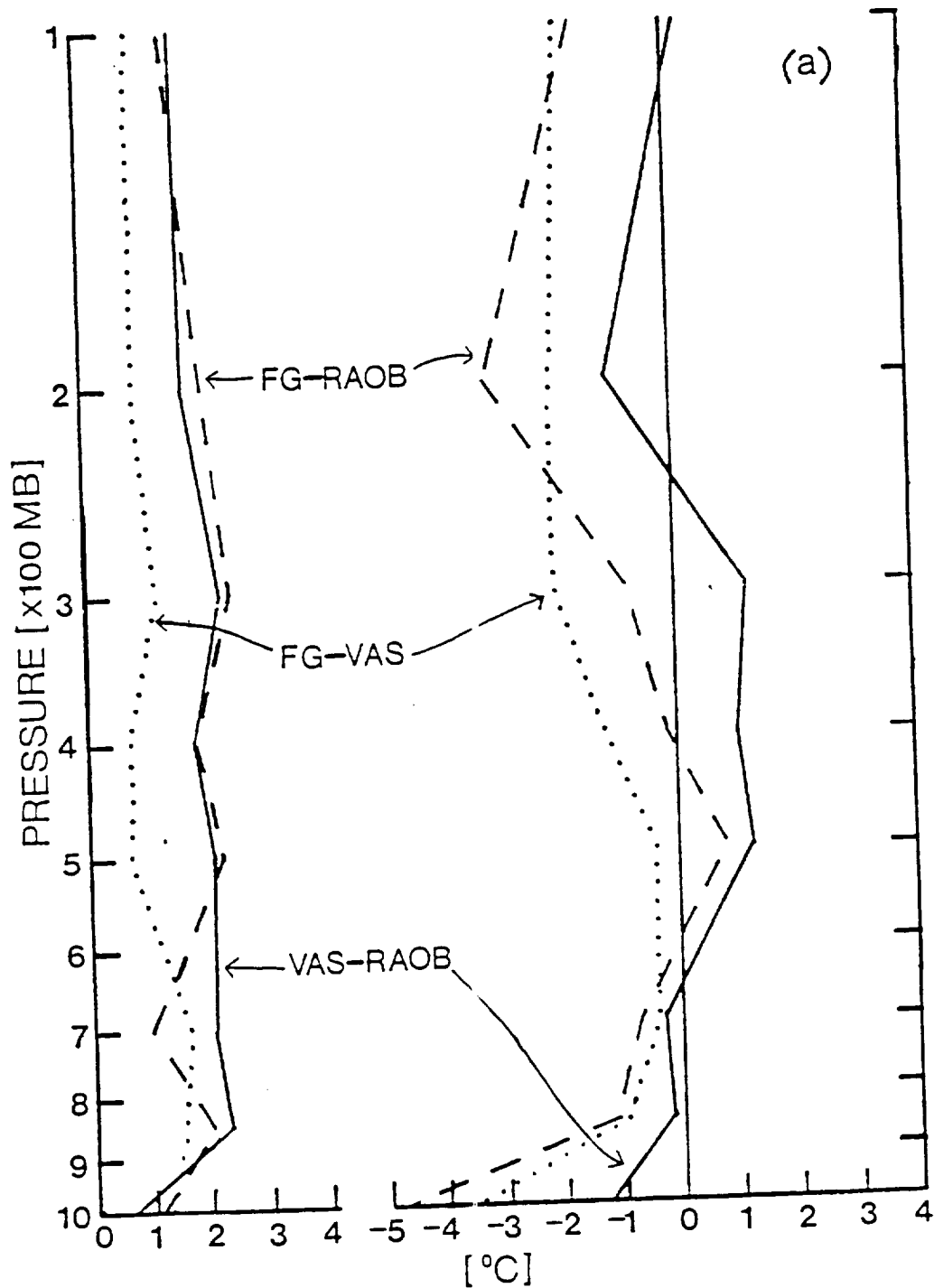
Fig. 6. Means (right) and standard deviations (left) of differences between paired sets of first guess and radiosonde data (FG-RAOB), VAS retrievals and radiosonde data (VAS-RAOB), and first guess and VAS retrievals (FG-VAS). Temperature results are in (a) while dewpoint results are in (b).
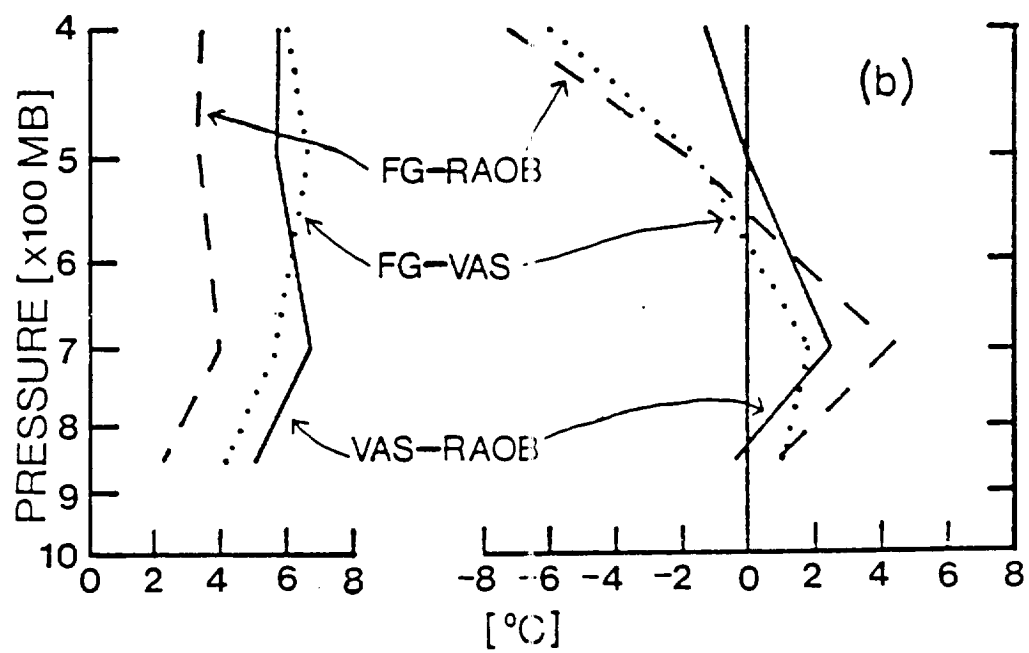
Fig. 6. (Continued)

Concerning mean arithmetic differences between VAS- and sonde-derived temperatures, the VAS-RAOB profile shows smaller differences than the FG-RAOB profile below 700 mb. This means that the VAS retrievals are closer to the ground truth than are the guess profiles from the LFM. Conversely, however, the FG data are closer to observed values between 700-300 mb. Finally, above 300 mb, the VAS-RAOB profile once again exhibits the smaller mean difference. Absolute values of the mean differences are less than approximately $3^{\circ}C$, with the greatest (negative) differences being located near the surface and 200 mb where both the retrievals and guess profiles are colder than the verifying sonde data. The FG-VAS profile shows that VAS-derived temperatures are warmer than the guess values from which they were obtained, and that mean differences between the input and output data are less than $2^{\circ}C$.

Standard deviations of the FG-RAOB and VAS-RAOB pairings (Fig. 6) are very similar at most levels, approximately $2^{\circ}C$, except near 700 mb where the guess deviations are smaller $(1.1^{\circ}C)$. Above 500 mb, the retrievals agree better with the sonde data than do the guess values, but the improvement is less than $1^{\circ}C$. Nearer the surface, the guess profiles are slightly superior. Finally, the FG-VAS profile reiterates the small difference between the guess and retrieval data. Although the small contrasts between the guess and observed sonde data indicate that the LFM prognosis was quite good, it is somewhat surprising that the algorithm was only able to improve it by such a small amount.

Pairing results for the composite dew point data (Fig. 6) are very interesting. It is encouraging that mean differences for the VAS-derived values are smaller than those of FG data at most levels; however, standard deviations of differences are very large. The smaller standard deviations of the FG-RAOB pairings are partly attributable to the smoothness of the LFM dew point patterns, although even those deviations are approximately $3.5^{\circ}C$. Firm conclusions cannot be made from these results alone due to the large deviations.

Current results are consistent with those of Jedlovec (1985), who compared gridded data over only the mesoscale radiosonde network over Texas. The fact that VAS results are most accurate above 300 mb and below 700 mb may be due to VAS's limited resolution in the middle levels coupled with the occurrence of a major temperature inversion at those levels during the period.

D.    Correlation Function Analyses

The second mode of evaluating the satellite retrievals employed structure and correlation analysis. Both isotropic and anisotropic functions were calculated for individual times and for an all time composite, and these calculations were made for all twelve VAS channels. For brevity, only examples of these results are presented here. To enable FG and VAS data to be compared with the brightness temperatures, weighted averages of the sounding profiles were prepared. The goal was to simulate the layer average that would be detected by the various VAS channels. As the first step, representative RAOB soundings for the period were input to a radiative transfer algorithm, yielding a satellite weighting function for each of the twelve channels. The weighting functions at individual locations were averaged and then normalized to a range of 0.0-1.0. Thus, a composite weighting function was formed for each channel. Then, at the various sounding sites, values of FG or VAS temperature at the surface and mandatory levels were multiplied by the weighting function. These weighted averages were used in the structure and correlation functions as FG or VAS layer equivalents to BT. For the water vapor channels, precipitable water values were calculated at each site over the layers 850-700, 700-500, 500-400, and 400-300 mb. The values then were multiplied by the normalized weighting function to form the weighted average. The resulting precipitable water was used in the subsequent calculations of FG and VAS layer equivalents.

1. <u>Thermal</u> <u>Channels</u>

Results for Channel 6 (4.5 microns) at 0235 GMT 7 March are given to represent the seven $CO_2$ thermal channels. During the current period, the weighting function for this channel peaks broadly between 500 to 700 mb. Figure 7 shows contoured fields of BTs, FG layer equivalents, and VAS layer equivalents. BT is contoured in units of brightness temperature, while FG and VAS layer equivalents are contoured in units of ambient temperature. Since BT is physically different from FG and VAS, one should not visually compare its gradient strength with those of the other two. Gradient orientations, however, can be compared visually, and correlation functions are used in later paragraphs to evaluate gradient strengths. Notice that the FG field has a smooth, well-defined thermal trough while BT and VAS have noisier, less organized patterns with isotherms oriented in a more east-west direction. The VAS isotherm configurations appear most similar to isopleths of the BT field.

Figure 8 contains anisotropic correlation functions corresponding to the analyses in Fig. 7. When interpreting anisotropic correlation functions, the orientation of
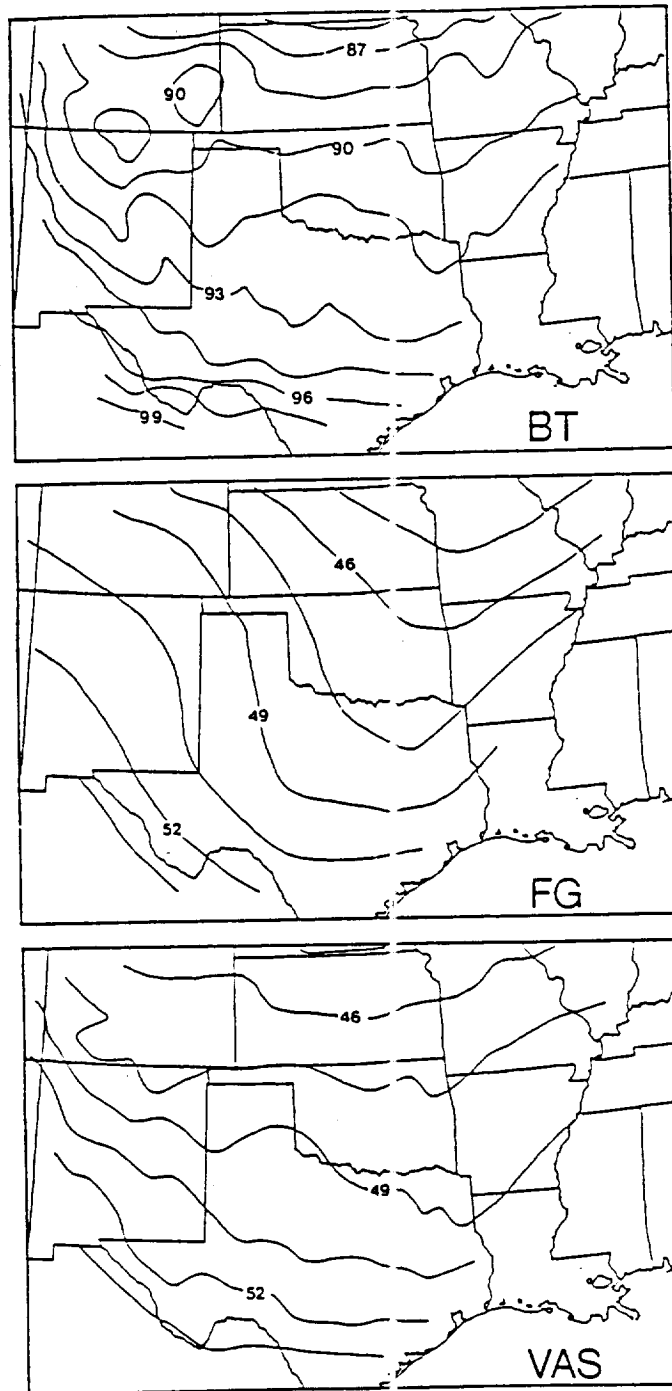
Fig. 7. Horizontal analyses relating to Channel 6 at 0235 GMT 7 March. On the FG and VAS panels, 52 represents 252 K ambient temperature. On BT, 90 represents 290 K brightness temperature. Contour intervals are 1.5 K.
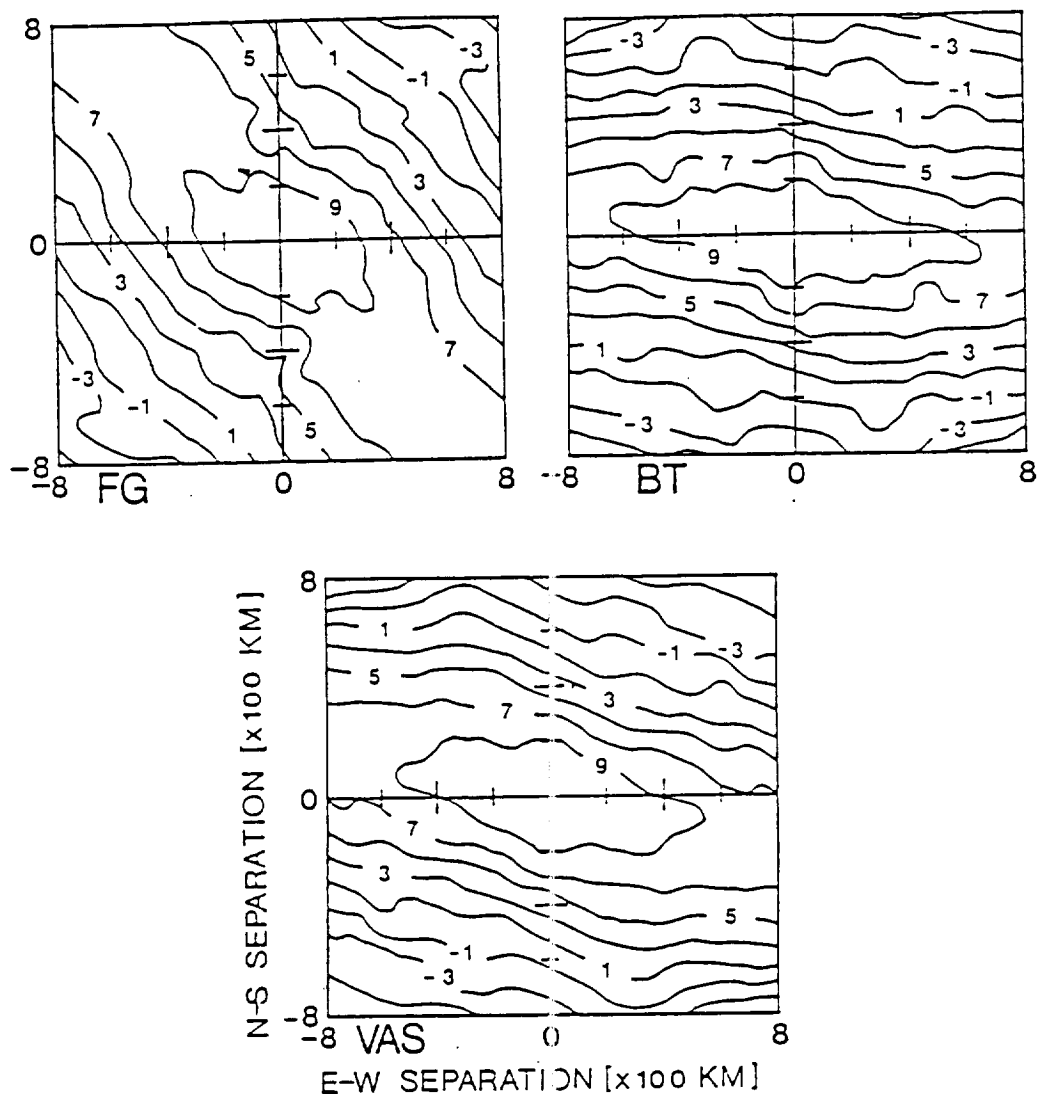
Fig. 8. Anisotropic correlation functions pertaining to VAS Channel 6 at 0235 GMT 7 March. Functions are for the first guess layer equivalent, brightness temperature, and the VAS layer equivalent. Contour label of 1 denotes 0.1 correlation.

isopleths must be considered. Most anisotropic depictions in this study have well defined axes of maximum correlation, with the strongest gradients being perpendicular. In the special case of isotropic data, however, there is no preferred direction of correlation, and the isopleths appear circular. Strong gradients along a particular direction are indicated by a close spacing of the isopleths in that direction.

In Fig. 8, one should notice that all three fields are highly anisotropic; that is, there are preferred directions of maximum gradient and maximum correlation. Also, gradient orientations here agree with those of the analyses (Fig. 7). Specifically, the axis of the BT function runs from just north of due west to just south of due east. On the other hand, the axis of the FG function is aligned northwest-southeast. Finally, the axis of the VAS function is oriented west-northwest to east-southeast, or between the BT and FG functions but slightly closer to that of BT. This suggests that BT is contributing somewhat more information to gradient orientations than does FG, although there is some blending or compromise between the two. This is seen often in the other temperature channels, but not universally. In terms of gradient strength, it still is difficult to tell which input is providing the most information since as all three are quite similar.

The smoothness of the correlation functions and horizontal analyses should be investigated. Although small-scale features were present in BT and FG/VAS layer equivalents during the study period (Fig. 7), the statistical scheme appears to filter them out. Another aspect is that normal usage of satellite data involves specific levels, while the BT data and the FG/VAS equivalents examined here are layer-averaged quantities.

Figure 9 shows FG and VAS-derived temperature fields at 500 and 700 mb. When compared to the equivalents (Fig. 7), it is apparent that the level data have more detail and stronger gradients, especially with the VAS data. Since the layer equivalents are weighted averages of data at these and other levels, it appears that the vertical averaging that formed the layer equivalents has removed many of the small-scale features. An important additional point is that the VAS temperatures at 500 and 700 mb have more detail than either the BT or FG fields from which they were derived.

The visual appearance of vertical smoothing (Figs. 7 and 9) is objectively confirmed by structure function-derived random error values for the layer equivalents and component levels (Table 1). Beven (1988) describes procedures for the error estimation. With the FG data, the random error of the layer equivalent is between the maximum and minimum errors for the individual levels, thereby indicating the vertical averaging that results in error reduction. Of course, the LFM-based FG fields are expected to be broad scale, even at

(a)
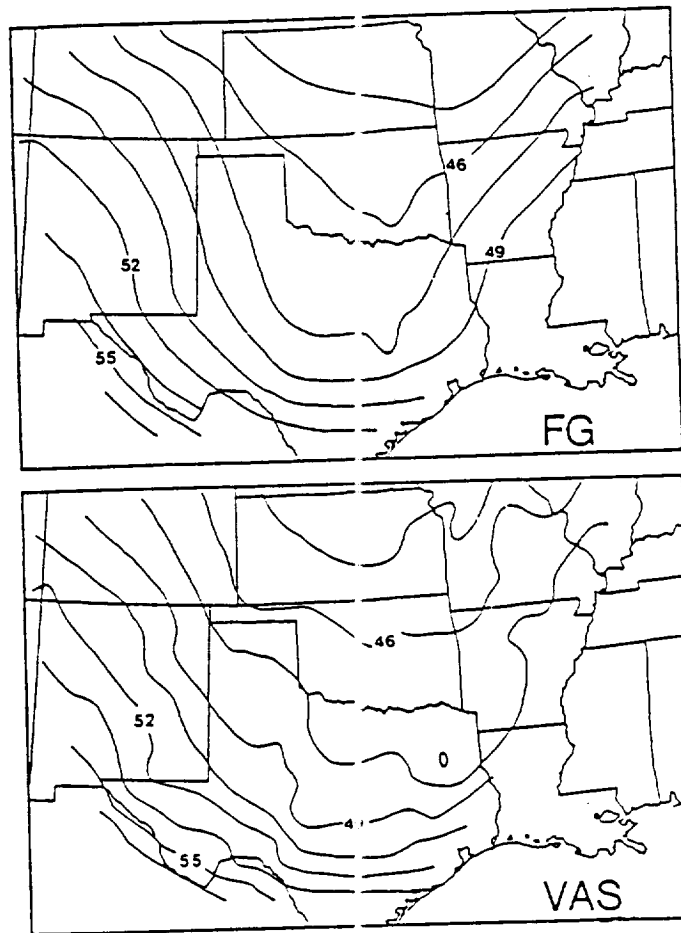


Fig. 9.  As in Fig. 7, except for FG and VAS 500 (a) and 700 mb (b) temperatures at 0235 GMT 7 March.

(b)
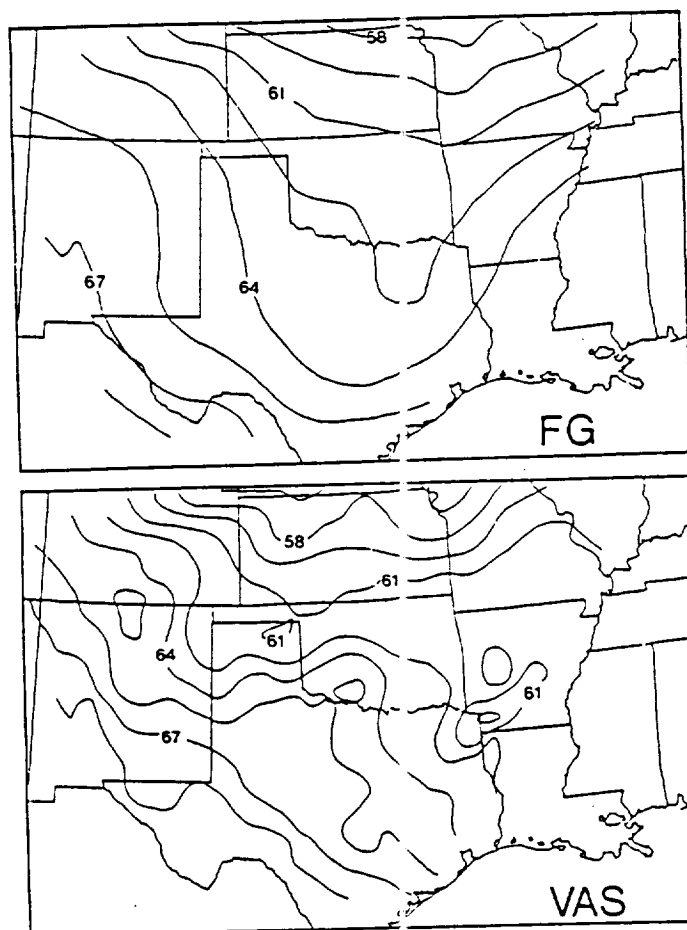


Fig. 9. (Continued)

Table 1.  FG and VAS random temperature (T) errors in Kelvins for layer equivalents and individual levels at 0235 GMT 7 March.

| Parameter | Error (K) |
| --- | --- |
| **First Guess:** | |
| Channel 6 Equivalent | 0.288 |
| 850 mb T | 0.257 |
| 700 mb T | 0.276 |
| 500 mb T | 0.429 |
| 400 mb T | 0.524 |
| **VAS:** | |
| Channel 6 Equivalent | 0.377 |
| 850 mb T | 0.682 |
| 700 mb T | 0.583 |
| 500 mb T | 0.517 |
| 400 mb T | 0.752 |

individual levels. For the VAS retrievals, notice that the error of the layer equivalent is less than the error of any of the input levels. This again indicates the vertical smoothing, yielding a layer equivalent with fewer small scale features than the level inputs.

Differences between the layer equivalents and component levels can also be seen in the anisotropic correlation functions. Figure 10 shows results for 700 and 500 mb VAS and FG temperatures. Orientations for the individual VAS levels are somewhat different from those of the layer equivalents (Fig. 8) although overall gradient patterns appear similar. There is much less difference between level and layer orientations of FG.

Fine-scale details of the VAS temperature fields at individual levels (Fig. 9) are not readily apparent in the correlation functions (Fig. 10). The reason is a limitation of the functions themselves. That is, the averaging of correlation values within distance ranges of 125 km acts as a kind of inherent filter since signals of features smaller than this amount are grouped together. (Beven (1988) gives details of the procedure.) Furthermore, much of the signal in the first separation bin is statistically interpreted as random noise in the structure function calculations, and is therefore removed from the correlation functions (Beven, 1988). Thus, the correlation functions do not reveal some of the smaller scale gradients, although they do describe the larger scale pattern. This would account for the fact that correlation functions at longer separations are similar.

The origin of fine-scale detail in the retrieval layer equivalents is not totally known, but the similarity of the BT and VAS equivalent fields suggests that some portion comes from the radiometric data. The VAS layer equivalent was calculated from individual levels having small-scale features. Since the BT field is inherently vertically averaged, the satellite sensor combines average radiances emitted by features at multiple levels into one brightness temperature. Thus, some portion of small-scale retrieval features may represent valid meteorological phenomena that are produced by the algorithm when combining together the data from several radiometric channels. Some other portion of the retrieval detail, especially that at individual levels, may be attributable to random noise due to unresolved cloud contamination, limitations of the retrieval algorithm, etc.

## 2.  Water Vapor Channels

VAS Channel 10 at 6.7 microns detects middle to upper tropospheric water vapor and is used frequently to find dry
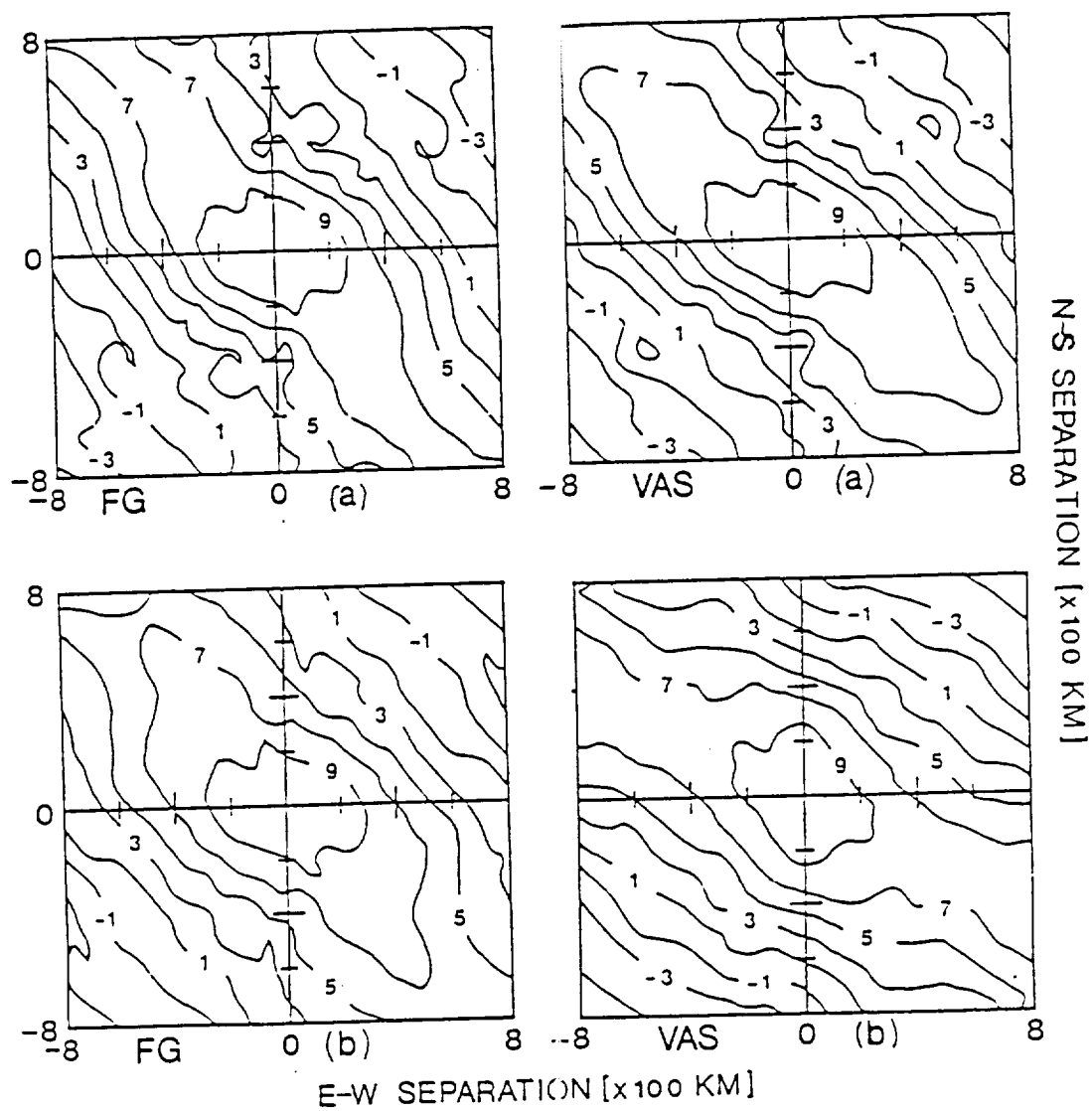
Fig. 10. As in Fig. 8, except for FG and VAS 500 (a)
and 700 mb (b) temperatures at 0235 GMT
7 March.

intrusions in severe storms situations and to identify circulation features that may not be associated with visible cloudiness. Results for Channel 10 at 0230 GMT 7 March are given to represent the three VAS water vapor channels.

Figure 11 shows contoured fields of Channel 10 BT, the FG layer equivalent, and the VAS layer equivalent. The LFM-derived FG layer equivalent has a smooth pattern with a well-defined dry slot running from central Missouri to central Texas. The VAS layer equivalent is somewhat similar in that a dry slot extends from near St. Louis, MO southwestward to south-central Texas, but the overall pattern has many more small-scale details, and the axis of dry air is less well defined than in FG. The dry feature in the retrievals corresponds to an area of warm brightness temperatures and to a dark streak on the water vapor image. The retrievals also depict comparatively humid air over southwestern Kansas, corresponding to cold values of BT. One should note that even though the FG layer equivalent had a dry slot forecast over the region, the BT and VAS positions are about 300 km southeast of the forecast location. This raises an important point when relating correlation functions to map analyses. That is, different locations of well defined features having similar gradients and orientations of gradients yield similar correlation functions, at least to the extent that the features are contained within the data network.

Anisotropic correlation functions (Fig. 12) quantify limitations of the humidity retrievals seen in the analyses (Fig. 11). First of all, the VAS axis of maximum correlation is approximately northeast-southwest, while that of FG is east-northeast to west-southwest and that of BT is just north of east to just south of west. In other words, the VAS axis is not intermediate to that of either input. In addition, one should notice VAS's poorly defined gradient pattern. Although 0235 GMT is the best example of noisy patterns, each of the VAS functions exhibits more small-scale detail than occurs in either FG or BT. Finally, one should note the parallel axes of positive and negative correlation in the FG function. They correspond to the half wavelength of the dry slot, about 600 km. Although similar features appear in FG and VAS functions at 0835 GMT 7 March (not shown), major differences in gradient orientations suggest that the VAS retrievals are not a simple reflection of the FG pattern.

Dew point analyses at specific levels further illustrate limitations of the water vapor retrievals. Figure 13 contains contoured fields of dewpoint data at 400 and 500 mb that were used to make the layer equivalents in Fig. 11. The smooth FG patterns are a major contrast to the extremely irregular VAS patterns. This contrast is typical of all levels and times of the water vapor study. As Fig. 11 indicates, even the vertical averaging used in producing the layer equivalents does not completely remove irregularities at the component levels. As with the temperature channels, the exact source of
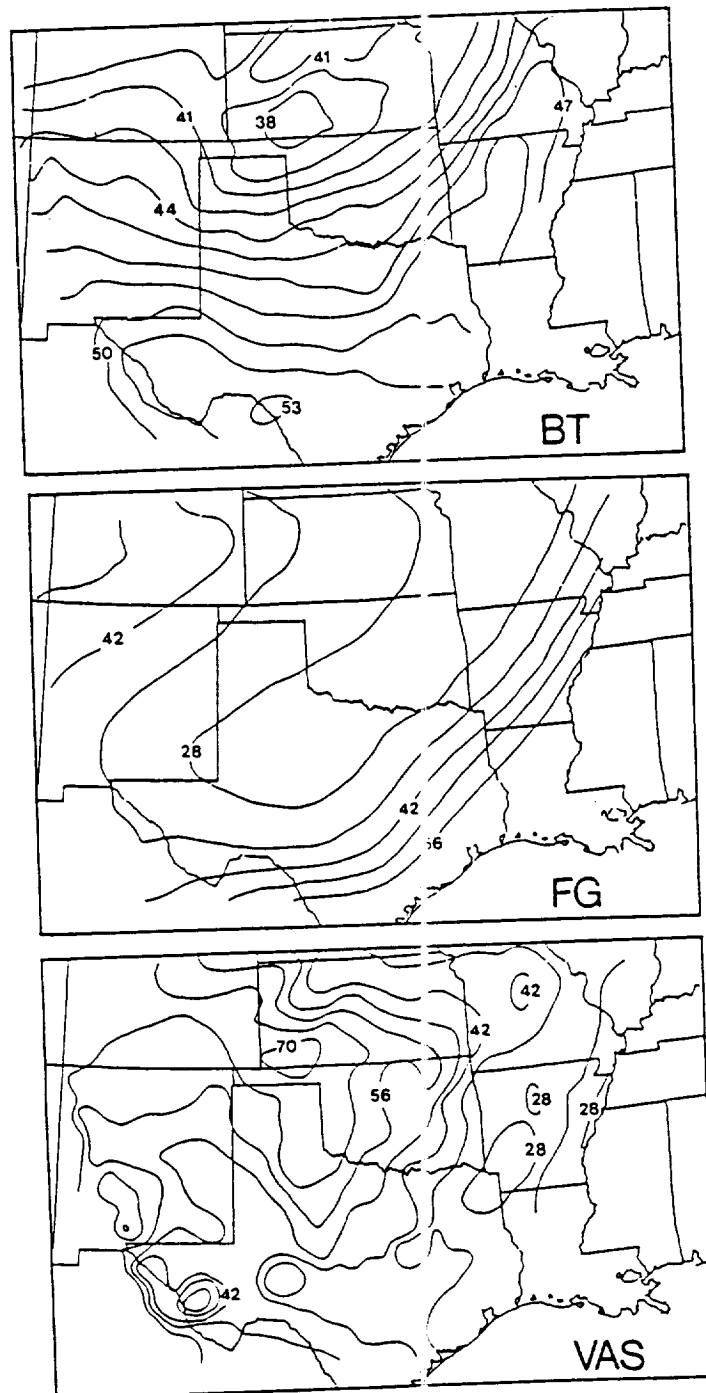
Fig. 11. Horizontal analyses pertaining to VAS Channel
10 at 0235 GMT 7 March. On the FG and VAS panels,
70 represents 0.7 mm of precipitable water. On
BT, 50 represents 250 K. Contour intervals are
0.07 mm and 1.5 K.
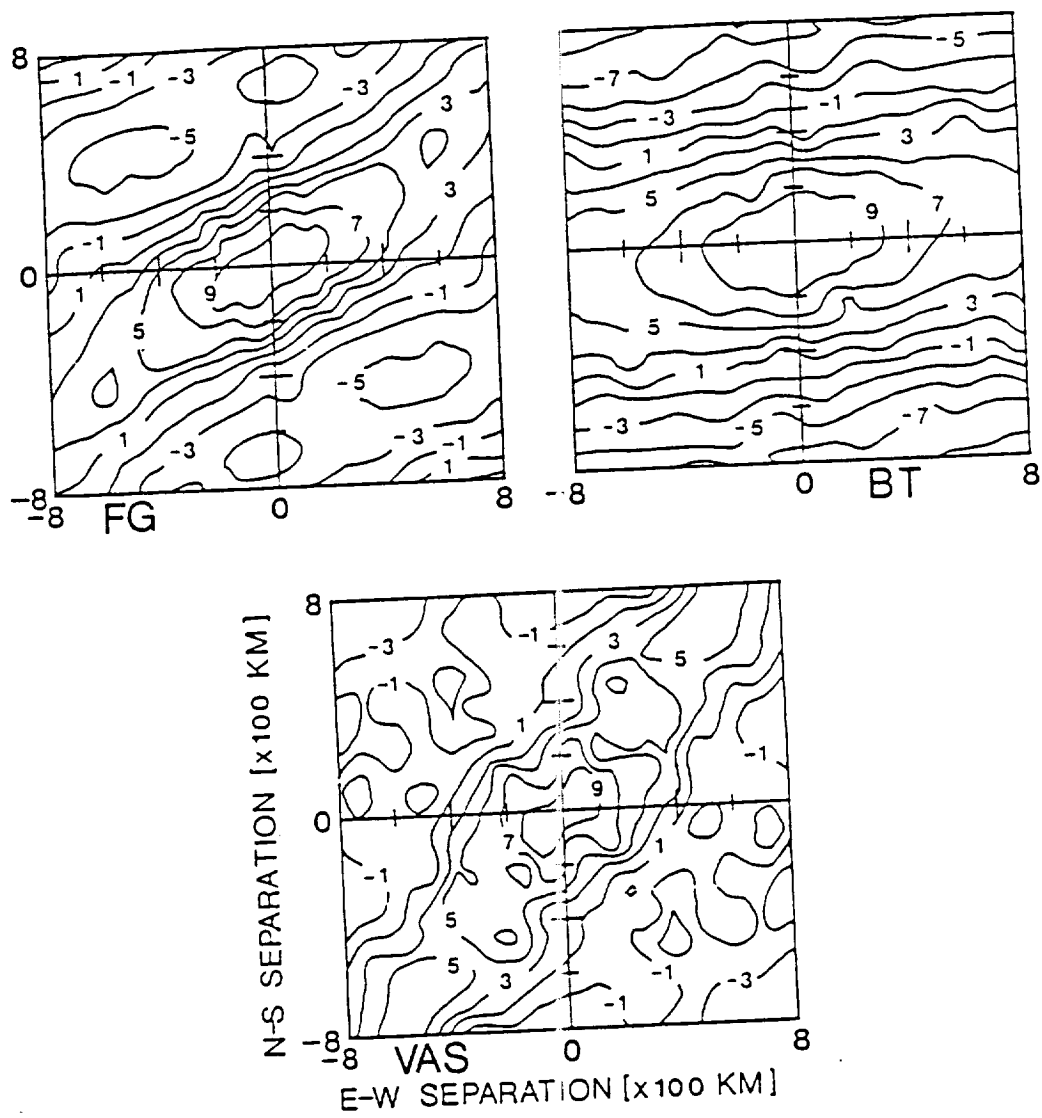
Fig. 12. As in Fig. 8, but for VAS Channel 10 at 0235 GMT 7 March.

(a)
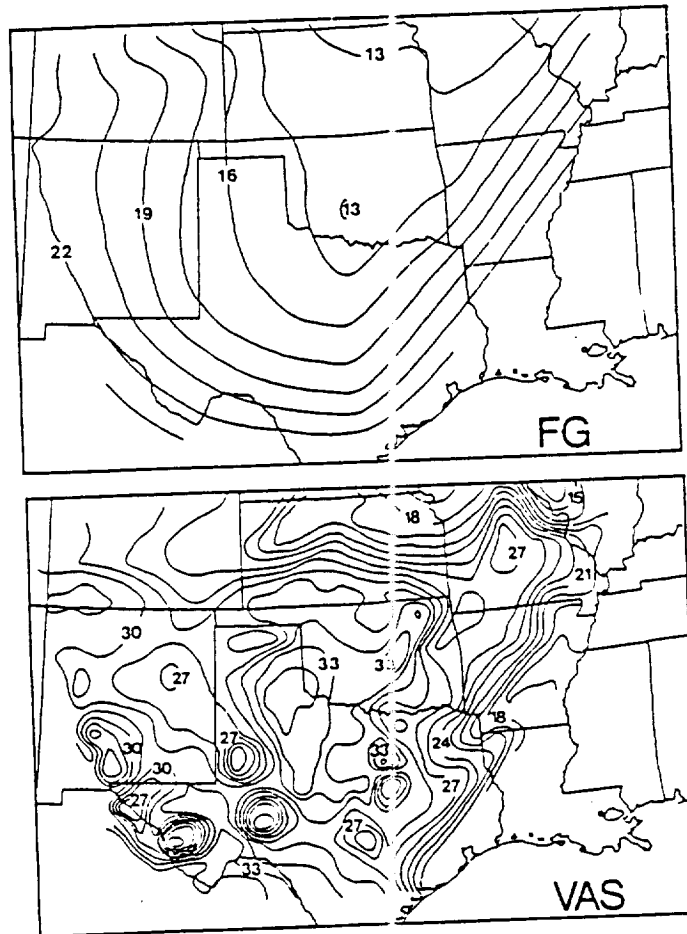


Fig. 13. As in Fig. 7, but for FG and VAS 400 (a) and 500 mb (b) dewpoint at 0235 GMT 7 March.

(b)
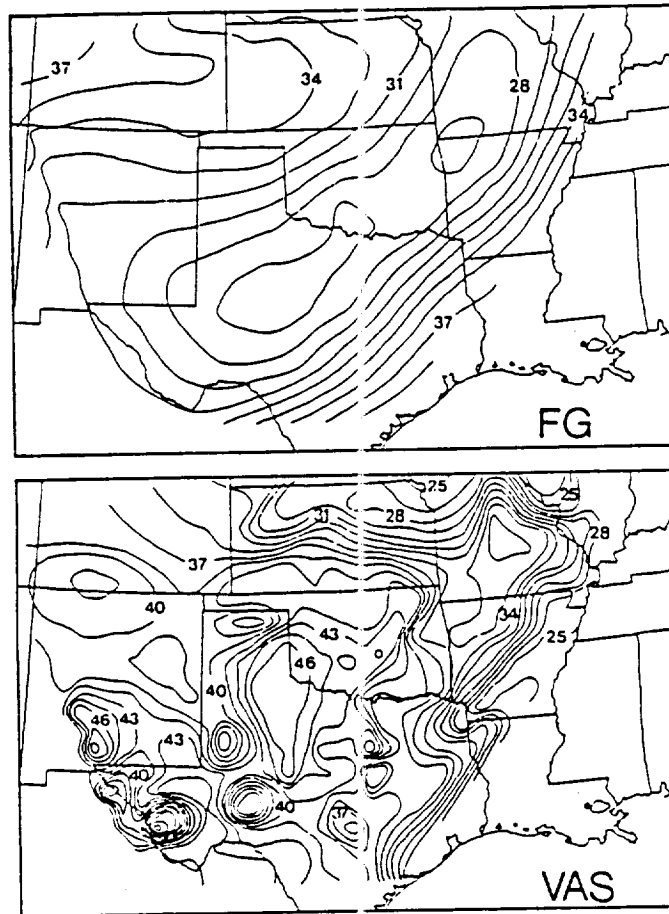


Fig. 13. (Continued)

the detail in the VAS level data is not known. Some may represent legitimate features arising from the algorithm's combining information from the three available radiometric channels. Once again, however, part of the detail may be attributable to limitations in the sensor, algorithm, cloud detection, etc. The fact that VAS contains only three water vapor channels increases the probability that the features are noise. Those investigators who have compared VAS humidity features to sonde-derived versions on 6-7 March have not reached a consensus as to the validity of the retrieval features (e.g., Jedlovec, 1985; Fuelberg and Meyer, 1986; Chesters et al., 1988).

To summarize, it appears that FG provides the most influence to the orientations of VAS gradients, whereas the placement of VAS geographical patterns most resembles BT. On the other hand, the excessive noise in the retrievals is not depicted in either input. The overall strength of VAS gradients appears to be a blend of both FG and BT.

## E.  Conclusions

By pairing satellite sounding sites with a special network of radiosondes, it was found that VAS-derived temperatures in the upper and lower troposphere were closer to the RAOB-derived ground truth than were the FG data. Conversely, FG soundings were closest to the ground truth in the middle troposphere. In general, the LFM first guess profile was good, and the retrieval algorithm could yield only little improvement. Moisture results from the pairings were dominated by large uncertainties. Standard deviations of dewpoint differences between FG, VAS, and RAOB were as large or larger than mean differences. This makes any comparisons of the moisture pairing results statistically meaningless.

Statistical structure and correlation functions were used to compare gradient information between VAS and its inputs of FG and BT data. It appears that the retrieval algorithm takes two smooth inputs, one at individual levels (FG) and the other a layer average (BT), and produces fields having considerably more detail. Much of the fine-scale detail evident at the individual levels was removed when vertical averaging was used to prepare the layer equivalents. The source for this detail is uncertain, but some may be noise, while some may legitimately arise when the algorithm combines the inherently vertically averaged brightness temperatures from all VAS channels. This part of the output may represent true meteorological features. The fact that patterns of VAS thermal layer equivalents seemed better related to FG equivalents and to BT, than FG at individual levels, suggests that one should use VAS data in a layer mode, e.g., thickness.

The tendency, unfortunately, has been to treat VAS and RAOB soundings similarly, i.e., using values at discrete levels.

The VAS, FG and BT fields were similar on the large scale, and although VAS was designed to add information on small-scale features, those that were apparent in analyses of both the layer equivalents and level data were not obvious in analyses of BT. Of course, it is possible that few small-scale features were present during this cold, stable period. In any event, the detail that was evident in the various analyses was not apparent in the corresponding correlation functions, which were often quite similar among the three types of data. This may be due to inherent averaging by the functions and the fact that some of the small scale detail is statistically interpreted as noise, thereby never appearing in the correlation functions.

In the case of moisture, correlation results showed the uncertainty revealed by the pairing procedure. Although some orientations of the three data types were similar, there were differences in terms of where the features were placed. Locations of FG and VAS dry tongues were separated by 300 km; however, VAS and BT positions were almost co-located. The middle-tropospheric vapor retrievals were very noisy, a characteristic not evident in either input. VAS uncertainty at individual pressure levels again appeared greater than in the layer equivalents. Thus, once again, layer integrated parameters such as precipitable water seem appropriate.

Based on the above, a major conclusion is that the radiometric data often did not appear to have a decisive influence on the final VAS temperature and humidity patterns and gradients for this case. In other words, broad-scale patterns and gradients of FG, BT and VAS often were similar. Smaller scale features in the retrievals had an uncertain origin. Thus, it was unclear whether they were a realistic outgrowth of the twelve channels or were due to uncertainty.

# IV. CASE STUDY OF PROCESSES RESPONSIBLE FOR

# OBSERVED PATTERNS IN 6.7 MICRON WATER VAPOR IMAGERY

## A. Introduction

Water vapor imagery has been available from geostationary satellites for nearly ten years. The 6.7 micron channel reflects the distribution of middle tropospheric water vapor where dark shades customarily represent warm brightness temperatures, i.e., dry conditions, and light shades represent moist areas. Past studies have employed water vapor imagery to diagnose winds and circulation patterns, enhance water vapor analyses, infer jet stream dynamics, and investigate tropopause folds. The current focus of research examined the atmospheric processes associated with the movement and further development of two pronounced dark (warm) features in a series of 6.7 micron images on 6-7 March 1982. Details are given by Moore (1987) and Moore and Fuelberg (1988) while highlights are presented here. The current research is an extension of work by Stewart and Fuelberg (1986).

## B. Meteorological Conditions

Figure 14 presents surface analyses, 500 mb heights and temperatures, and 300 mb isotachs subjectively analyzed from radiosonde data. At the surface at 0000 GMT 6 March 1982, a stationary front extended from the lower Rio Grande River Valley through the Gulf of Mexico and Southeast States into the Atlantic Ocean. Several weak low pressure waves were located along this front. A moderate area of high pressure was centered over Nebraska, and a secondary cold front stretched along the Canadian border. By 0000 GMT 7 March, the stationary front remained over the Southeast, extending into the Gulf of Mexico as a cold front. The secondary cold front advanced southward into Kansas. The high centered over Nebraska at the initial time moved south and diminished, while another anticyclone followed the secondary front.

Middle tropospheric analyses (Fig. 14) at 0000 GMT 6 March show a longwave trough extending from the Desert Southwest northeastward into the western Great Lakes. The trough propagated into the Southcentral States during the
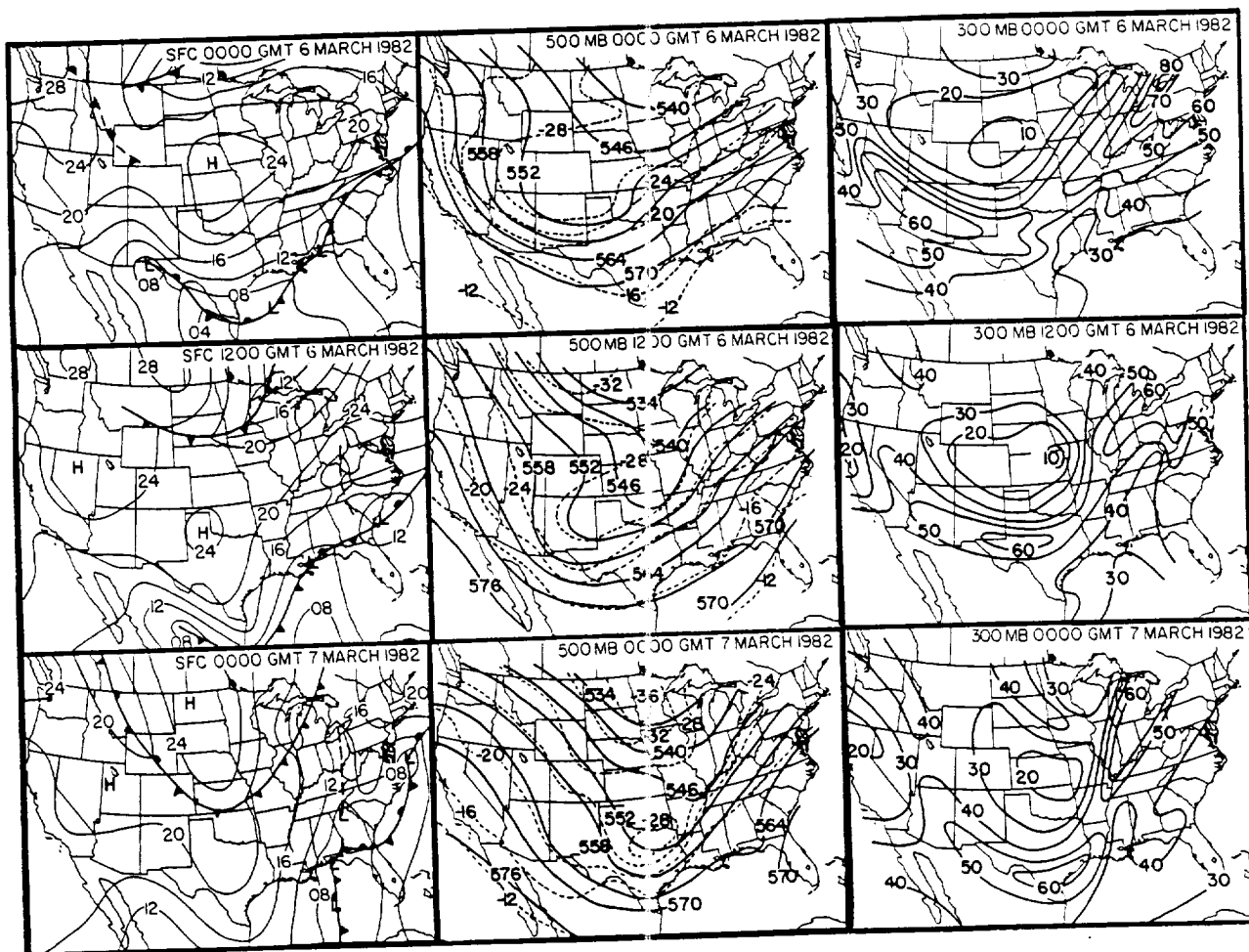
Fig. 14. Surface analyses (left column) with pressure in mb (20=1020 mb), 500 mb analyses (center column) with heights (540=5540 gpm, thick solid) and temperatures in °C (dashed), and isotachs at 300 mb in m/s (right column).

period, extending from Texas to Manitoba at the final time when a longwave ridge was evident over the West Coast.  Two weak shortwaves were embedded in the trough at 0000 GMT 6 March.  The one located over Oklahoma, just east of the base, intensified slightly while moving slowly downstream.  The second shortwave initially was over Arizona, slightly upstream of the trough axis, but then moved into the base and amplified considerably.  A shortwave ridge located over Idaho at 0000 GMT 6 March amplified and moved southeastward during the next 12 h; however, by 0000 GMT 7 March, it was near the longwave trough and smaller in amplitude.

Middle tropospheric temperature patterns at the initial time (Fig. 14) include a baroclinic zone over the Desert Southwest and a cold dome over the central Great Plains and Intermountain States.  By 0000 GMT 7 March, the baroclinic zone had intensified; both narrowing in width and increasing in length, and stretching from southwest Texas to Arkansas. As the cold dome moved southeastward, it diminished in area and exhibited warming, thereby suggesting subsidence.

At 300 mb on 0000 GMT 6 March  (Fig. 14), the axis of the polar jet stream extended from the Pacific Northwest through the Desert Southwest and Southcentral States into the Ohio River Valley.  The jet streak over the Ohio Valley had a peak value of 81 m/s.  The second streak, centered over the Desert Southwest at 0000 GMT 6 March, propagated to southern Texas by 0000 GMT 7 March.  Its greatest speed was approximately 67 m/s.  A subtropical jet stream was evident at 200 mb (not shown).  It generally was parallel to, but somewhat south of its polar counterpart.

Water vapor imagery (6.7 micron) for the study period is presented in schematic form in Fig. 15.  Patterns indicate that a pre-existing "dark band" and a developing "dark band" combined into one large image feature by the end of the period.  Specifically, at 0000 GMT 6 March, a dark band of relatively warm brightness temperatures stretched from the Pacific Northwest into the Desert Southwest, with darkest shades over the California-Nevada border.  This apparent center propagated at a nearly constant speed of 18 m/s and will be denoted as the "advective band".

Development of a new dark (warm) band feature and enhancement of the older advective band are both apparent at 1200 GMT 6 March (Fig. 15).  The advective component now over Nevada and Arizona had darkened, partly attributable to the decreasing zenith angle.  In addition, a new area, the "development band", extended from Kansas through Iowa into Wisconsin, with a less distinct band bisecting Oklahoma. These features over the Great Plains were only faintly evident 12 h earlier.

The advective and development sections combined into one large, dark feature by 0000 GMT 7 March (Fig. 15), although

37
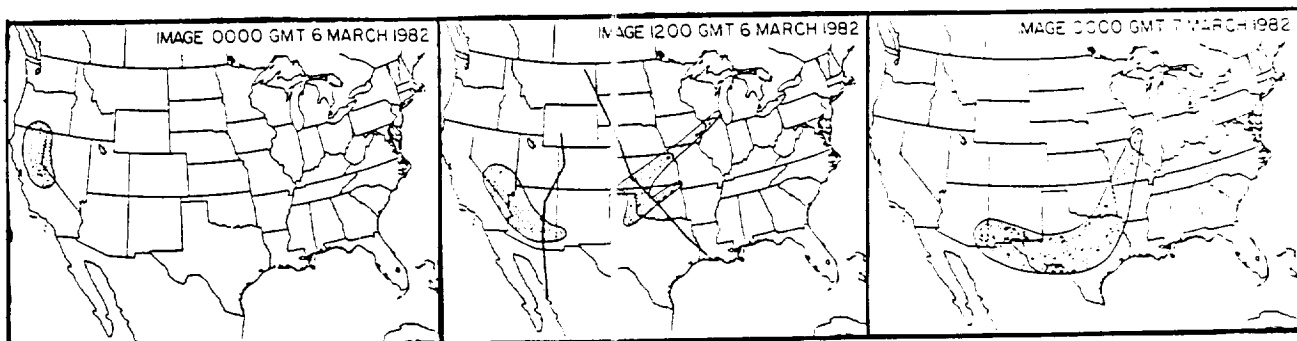
Fig. 15. Schematics of 6.7 micron warm, dark image features. Axes of cross secticns in Fig. 19 at 1200 GMT 6 March are shown.
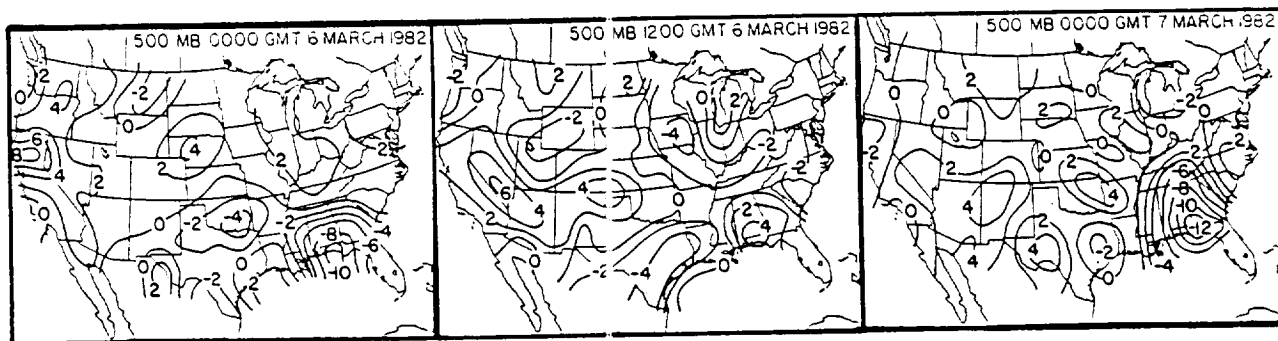
Fig. 16. Kinematic vertical motion at 500 mb (microbars/s).
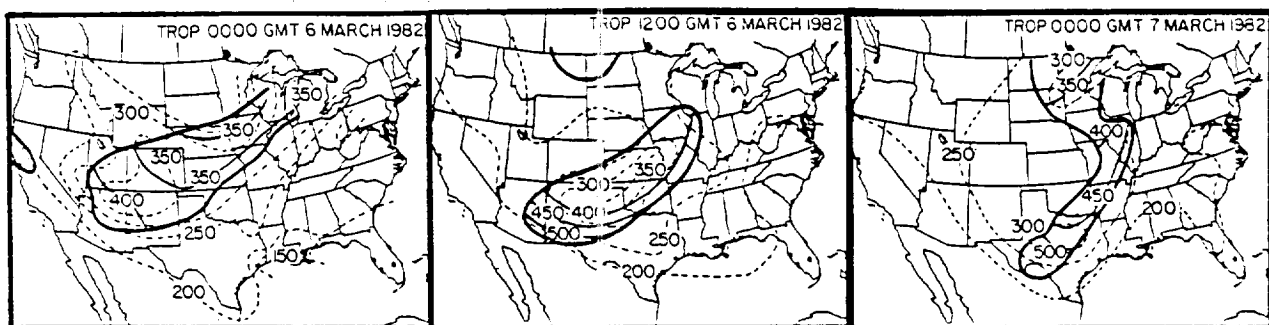
Fig. 17. Tropopauses reported by the National Weather Service in mb (dashed) and pressure topography (mb, thin solid) of the 304 K surface within the $10 \times 10^{-6}$ K/(mb s) isoline of potential absolute vorticity (heavy solid).

both preceding components were still distinguishable. The
development portion darkened (warmed) to the shade of the
advective section, extending from central Texas, northeastward
into Illinois. The advective section over southern New Mexico
and western Texas did not change its appearance.


C.  Results


1.  Isobaric Analyses


Before considering processes responsible for 6.7 micron
image features, moisture patterns were examined to confirm
their role in creating the observed imagery. Radiosonde-
derived dew point analyses at 500 mb (not shown) support the
accepted relation that the images primarily reflect middle
tropospheric water vapor distributions. Time sections (not
shown) constructed to diagnose vertical and temporal humidity
structures also support this conclusion.

To facilitate the calculation of other parameters,
radiosonde data at the surface and every 50 mb from 900 to 50
mb were objectively analyzed (Barnes, 1973). The response
function was selected to retain a conservative 50% of the
amplitudes of 800 km wavelengths (twice the data spacing).
Kinematic vertical motions were computed using centered finite
differences and were adjusted to zero at 100 mb based on the
O'Brien (1969) method.

Vertical motions at 500 mb are shown in Fig. 16.
Concerning the advective component of the image, the large
area of subsidence over northern California at 0000 GMT 6
March coincides with the darkest region (Fig. 15). This
subsidence is associated with the entrance region of the polar
jet streak (Fig. 14). Both the center of subsidence and the
image feature propagate to Nevada and Arizona by 1200 GMT 6
March, and two centers of descending motion are associated
with the dark band at 0000 GMT 7 March. The one over New
Mexico is associated with the polar jet, while the other, over
west Texas, appears to result from confluence north of the
polar jet.

The development section of the image (Fig. 15) also is
associated with subsidence (Fig. 16). At 0000 GMT 6 March,
there is descent over Nebraska, where the development
component is only faintly detectable. This subsidence is
located between the shortwave ridge and trough discussed
earlier. The descent strengthens at 1200 GMT 6 March while

39

translating to the southwestern edge of the image feature
(i.e., southeastern Colorado). Both the image band and its
associated subsidence are over the Ozark Plateau at 0000 GMT 7
March. The descent over southwestern Texas may also
contribute to formation of the development band.

To summarize, the isobaric analyses relate both the
advective and development components of the dark image feature
to subsidence. Isentropic analyses are the most advantageous
way to confirm and examine in greater detail the processes at
work in producing the image patterns.

## 2. Isentropic Analyses

An isentropic data set was created from the isobaric
version using a transformation procedure similar to that
outlined in Reiter (1972). Isentropic levels were at 2 K
intervals from 270 to 424 K. Potential absolute vorticity
(PAV) was used to diagnose tropopause folding, i.e., air of
recent stratospheric origin in middle and upper tropospheric
fronts. PAV is the product of absolute vorticity (AV) and
static stability (SS) on isentropic surfaces. Shapiro (1970)
stated that PAV greater than $10 \times 10^{-6}$ K/(mb s) represents
stratospheric conditions. Thus, a tropopause fold is denoted
by these values extending into the middle tropospheric, i.e.,
approximately 500 mb.

Figure 17 contains pressures of the National Weather
Service (NWS) reported tropopause based on the standard
definition involving temperature lapse rate. Also shown are
pressures of the 304 K surface where PAV indicates
stratospheric values. Other surfaces that were examined
exhibited patterns similar to those at 304 K. At 0000 GMT 6
March, the axis of stratospheric PAV is oriented northeast-
southwest, which, as expected, is coincident with the axis of
the cold dome (Fig. 14). Stratospheric PAV corresponds to
both the cold dome and baroclinic zone through the remainder
of the period. One should especially note the correspondence
between PAV and the development section of the image band over
the Great Plains (Fig. 15).

The pressure distribution of stratospheric PAV on 304 K
at the first time (Fig. 17) indicates that stratospheric
values reaching approximately 350 mb still are near the
traditionally reported tropopause level (350 mb). The only
exception is the extreme southern section of the enclosed
region where the 430 mb PAV altitude is lower than that of the
standard tropopause. An evolution over the southern region is
apparent by 1200 GMT 6 March, when stratospheric values now
extending to 500 mb are well below the standard tropopause
(250 mb). On the other hand, values over the northern portion

of the enclosure still are near the standard tropopause (360 mb). At 0000 GMT 7 March, stratospheric PAV continues to reach beyond 500 mb, extending at least 100 mb below the NWS tropopause. It is important to note that this delineation of the tropopause fold extending from Texas northeastward to Illinois is coincident with the dark, dry band of the 6.7 micron image (Fig. 15). The implication of Fig. 17 is that air now in the troposphere is of recent stratospheric origin, and should have the stratospheric properties of large PAV, high ozone concentration and low water vapor content (Danielsen, 1968).

Magnitudes of PAV on 304 K (Fig. 18, right column) were observed to steadily diminish through the 24 h period. This decrease is due to a reduction in static stability (Fig. 18, center column) coupled with near constant absolute vorticity (Fig. 18 left column). A decrease in SS should be offset by increasing AV (Uccellini et al., 1985). In this case, however, the response function of the objective analysis may be partly responsible for the constant, not increasing, AV. Specifically, observed horizontal wind gradients strengthened during the period, whereas the analyzed versions sometimes were not increased to the values observed. Unfortunately, the response function could not be altered to better resolve these gradients without introducing noise into the remainder of the analyses. Uccellini et al. (1985) also noted that analysis deficiencies may produce non-conservative PAV, and it has been observed below the level of maximum wind in frontal zones (Gidel and Shapiro, 1979), and resulting from diabatic processes (Staley, 1960).

Figure 19 contains cross sections through the advective and development components of the image. The cross section (top) through the advective feature at 1200 GMT 6 March is similar to those at other times. The extension of stratospheric PAV penetrates to 520 mb between Winslow (INW) and Tuscon (TUS), Arizona, signifying a tropopause fold that is coincident with the image (Fig. 15). The conventional NWS tropopause is located near 200 mb (Fig. 17) over this region.

Cross sections through the development feature at 0000 GMT 6 March (not shown) indicate a zone of enhanced horizontal wind shear, but no strong temperature gradient. Stratospheric PAV exhibits only a slight depression in the shear zone, remaining above 400 mb. By 1200 GMT 6 March (Fig. 19 bottom), on the other hand, the tropopause folding process is well underway over Oklahoma City (OKC), near the development section of the image band. Strong temperature gradients and wind shear are both quite apparent between OKC and Longview (GGG), Texas, producing an extension of stratospheric PAV down to 470 mb. The fold is fully developed at 0000 GMT 7 March (not shown), and is coincident with the development band.

Ozone measurements have been related to tropopause folding in several previous studies (e.g., Danielsen, 1968).

41
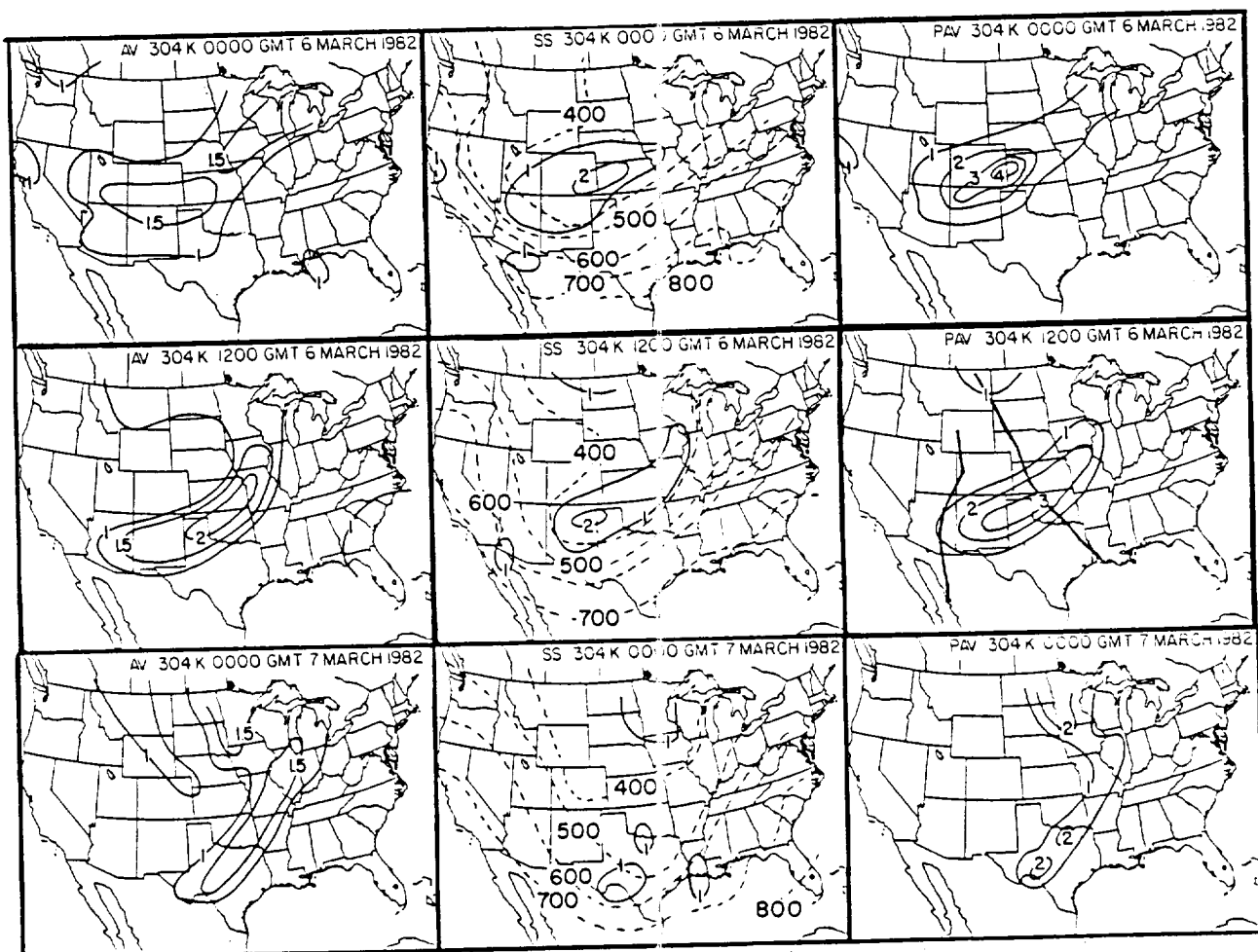
Fig. 18. Isentropic analyses on 304 K of absolute vorticity (AV, left column $1.5 = 1.5 \times 10^{-4}$ s$^{-1}$), static stability (SS, center, $2 = 20 \times 10^{-2}$ K/mb), and potential absolute vorticity (PAV, right column, $1 = 10 \times 10^{-6}$ K/(mb s)). Pressures of the 304 K surface are given in the center panels as dashed lines. Axes of cross sections in Fig. 19 at 1200 GMT 6 March are shown in right column.

42

1200 GMT 6 MARCH 1982

1200 GMT 6 MARCH 1982
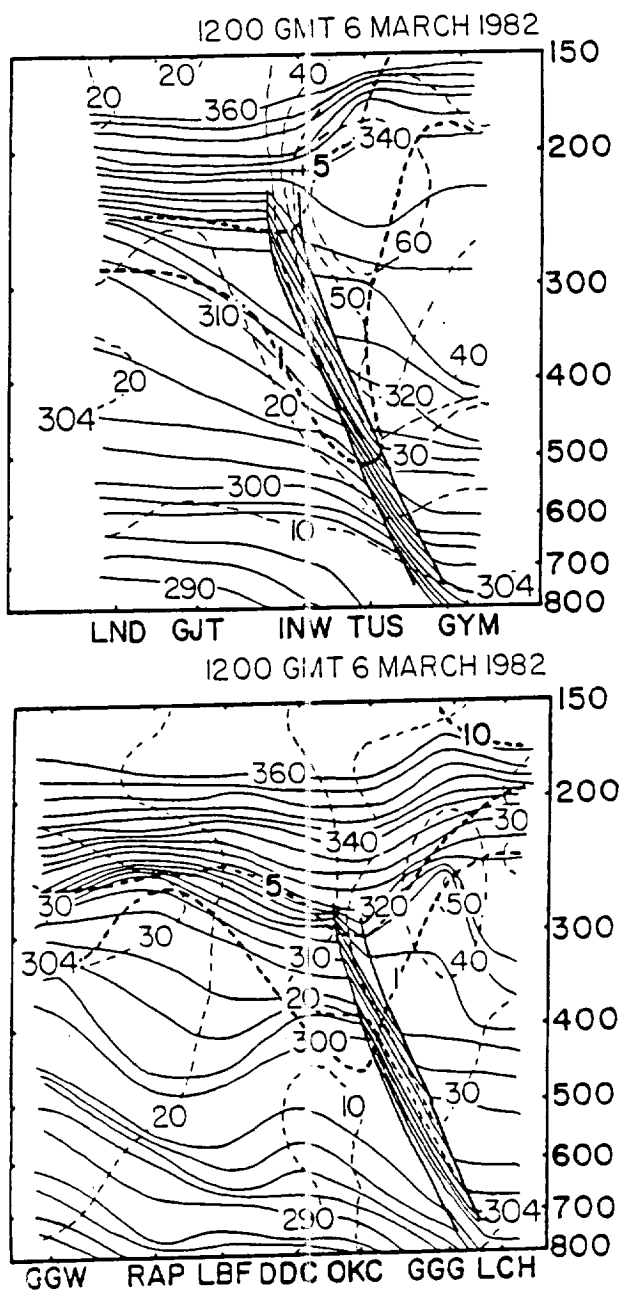
Fig. 19. Cross sections through the advective (top) and development (bottom) image bands with potential temperature (K, solid), wind speed (m/s, thin dashed), and potential absolute vorticity (1=10x10$^{-6}$ K/(mb s), thick dashed) for 1200 GMT 6 March. Axes are shown in Figs. 15 and 18.

43

Uccellini et al. (1985) noted that TOMS (Total Ozone Mapping Spectrometer) data can be useful "in that maximum ozone concentrations indicate a relatively thick stratosphere and correspondingly thinner troposphere." At 1700 GMT 6 March (Fig. 20), the TOMS data indicate a deep stratosphere over northeastern Texas (410 Dobson Units), with the axis of maximum concentration extending from Texas northeastward to Illinois. It is significant that this location is coincident with the area of stratospheric PAV on the 304 K surface (Fig. 17) and the development image component (Fig. 15) between 1200 GMT 6 March and 0000 GMT 7 March. This is further evidence of a tropopause fold over the central United States.

## 3. Isentropic Trajectories

To obtain a three-dimensional representation of processes responsible for the image features, isentropic backward trajectories were constructed using the implicit technique of Danielsen (1961). Figure 21 presents a sample of trajectories for both the advective and development image bands on the 304 K surface.

The trajectories terminating in the advective image feature were constructed between 1200 GMT 6 March and 0000 GMT 6 March. Figure 21 indicates that air ending over central Arizona at 544 mb originated near Ely, Nevada at 412 mb. This descent of 132 mb over 12 h corresponds to an average vertical motion of 3.1 microbars/s. Results for other trajectories in the advective band are similar. These parcels conserve their potential absolute vorticity, having values characteristic of tropospheric air.

Similar to results just described, backward trajectories between 0000 7 March and 1200 GMT 6 March (Fig. 21) reveal considerable descent near the development image band. For example, air at 447 mb near Monett, Missouri, at 0000 GMT 7 March originated 12 h earlier at 370 mb near Dodge City, Kansas. Corresponding subsidence also is evident in other nearby trajectories. Although PAV is not conserved, decreasing from 16 to 11 x $10^{-6}$ K/(mb s), stratospheric values are maintained. It should be noted that non-conservation of PAV is not unusual and has been encountered by many investigators (e.g., Danielsen, 1968). In the current work, it may result from the objective analysis deficiencies noted earlier.
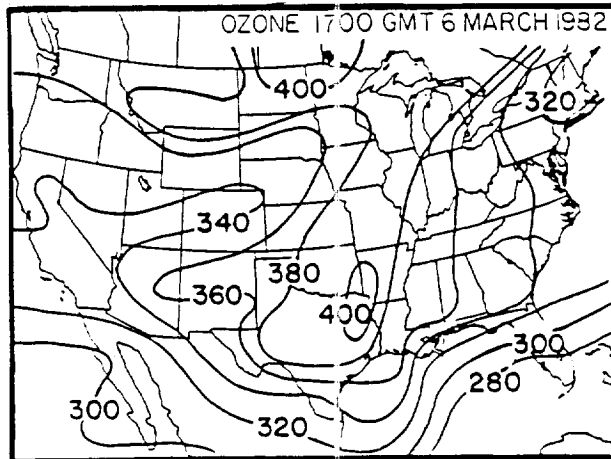
Fig. 20. Ozone data from the Total Ozone Mapping Spectrometer
(TOMS) in Dobson units for 1700 GMT 6 March.
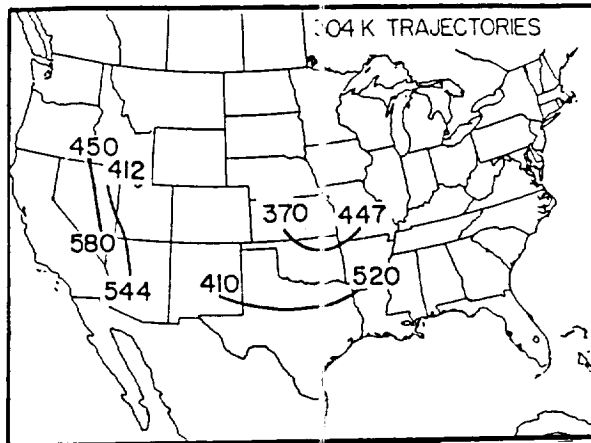


Fig. 21. Backward trajectories on 304 K for the advective
image band from 1200 to 0000 GMT 6 March (left), and
development band from 0000 GMT 7 March to 1200 GMT
6 March (right). Heavy numbers denote beginning and
ending pressures (mb).

## D. Conclusions

The dark, warm image bands in 6.7 micron water vapor imagery on 6-7 March 1982 were due to subsidence. Specifically, the advective band was produced by descent associated with the entrance region of a polar jet streak. On the other hand, the evolution of the development image component was coincident with a tropopause fold and associated intrusion of dry stratospheric air into the middle troposphere. Although not described here, we have successfully simulated these increasing brightness temperatures by altering upwind soundings based on trajectory-determined vertical motion, and then using both the original and altered profiles as input to a radiative transfer model.

# V. A SIMULATION AND DIAGNOSTIC STUDY OF

# WATER VAPOR IMAGE DRY BANDS

## A. Introduction

A promising new area of research into satellite imagery incorporates numerical modeling techniques. Specifically, regional models can provide important "data" for diagnostic meteorological studies (Keyser and Uccellini, 1987), yielding resolution unobtainable from the operational radiosonde network. This aspect of our research was part of a cooperative effort between NASA's Marshall Space Flight Center (see Kalb et al., 1987) and Florida State University. It combined the idea of using mesoscale model output as a high resolution data set with the concept of synthetically generating water vapor images. Specifically, model soundings of temperature and humidity served as input to a radiative transfer model that simulated satellite detected radiances and brightness temperatures in the 6.7 micron band. The technique was used for a case study of 6-7 March 1982 to investigate atmospheric processes associated with specific image features. This period is identical to that described in the previous chapter, where observed data were employed. Details are given in Muller (1988) and Muller and Fuelberg (1988) while highlights are presented here.

Previous research employing numerical models to diagnose satellite imagery includes the study by Rodgers et al. (1976) that used a ten level diagnostic model to quantitatively associate tropospheric dynamics with radiometrically observed water vapor features. Numerical models also have been used to forecast water vapor imagery. The Petersen et al. (1984) isentropic prediction scheme produced forecasts of VAS water vapor fields that captured some aspects of differential moisture advection leading to convection, but was inherently unable to simulate an observed increase in brightness temperature (TB) attributed to subsidence. More recently, Durran and Weber (1988) used a numerical model to simulate cirrus cloud shields associated with midlatitude jet streams.

# B. Methodology

Data for the 6-7 March 1982 period included observed VAS
6.7 micron TB's, radiosonde reports (RAOBs) from the VAS
Demonstration Experiment and model output from the Limited
Area Mesoscale Prediction System (LAMPS). The model output
was identical to that from the convective parameterization
experiment performed by Kalb (1987) and was prepared by
scientists in the Remote Sensing Branch of NASA's Marshall
Space Flight Center. The model simulation was initialized
with RAOB data from 1200 GMT soundings, and covered the period
from 1200 GMT 6 March to 0400 GMT 7 March 1982. History tapes
containing basic model variables and precipitation related
parameters at hourly intervals were processed to provide
vertical soundings of temperature, pressure, and humidity at
each model grid point for times corresponding to GOES/VAS
images. Image calculations were made from the LAMPS soundings
every three hours from 1200 to 0300 GMT, corresponding to VAS
imagery at 1100, 1430, 1730, 2030, 2330, and 0230 GMT. RAOBs
used in trajectory calculations were available at 1100, 1445,
1745, 2045, 2345, and 0245 GMT.

LAMPS has been described by Perkey (1976). The version
employed here had 15 sigma-height levels in the vertical, a
horizontal grid spacing of approximately 70 km, fixed sponge
boundaries, and fourth order diffusion to damp high
frequencies and noise. Vertical velocity was calculated by
vertical integration of the continuity equation subject to the
constraint that values equal zero at the bottom and top of the
model atmosphere. The model domain for the study was $23.625°$
to $43.625°$ N latitude and $107°$ to $80°$ W longitude. A modified
form of the radiative transfer code by Weinreb and Hill (1980)
was employed to simulate satellite-derived radiances for the
6.732 micron wavelength. Continuum and trace gas
contributions were ignored, and no provision was made for
model cloud areas. Humidity was set to zero above 100 mb, and
non-nadir viewing by GOES was included.

Once model radiance fields were calculated at the LAMPS
gridpoints, a two dimensional smoothing operator was applied
to suppress noise that appeared at later times of the run.
Comparison of observed to model TB was facilitated by
objectively analyzing the observed VAS images onto the LAMPS
grid. A subgrid representing an area common to both data
sources was utilized, and the Barnes (1973) scheme was used
for the analysis.

Radiances from cloudy areas are strongly affected by the
cloud tops and do not properly represent the vapor content of
the atmospheric column. Clouds in the observed VAS images

48

were located using a "split window" technique (Smith, 1983).
Model cloud areas were delineated by checking each grid point
for cloud water content greater than zero, starting at the top
level and working down.  If cloud water was found above the
750 mb level, the grid point was denoted as cloudy at the
middle and upper model levels.

Kinematic vertical motions were calculated from the
observed RAOB data.  The wind components were first
objectively analyzed onto a grid using the Barnes (1973)
procedure.  Then, after applying the kinematic algorithm, the
motions were adjusted based on O'Brien (1969), assuming that
values were zero at the surface and 100 mb.  Trajectories were
estimated from both the model and the observed wind fields
following the procedure outlined by Heckley and Hoskins
(1982).  This is an extension to three dimensions of
Petterssen's (1956) iterative technique.

The synoptic situation was described in the previous
chapter and will not be repeated here.  One should note,
however, that the current numerical study considered a more
limited horizontal area and a smaller time interval.


C.  RESULTS


1.  Comparison of Image Features

Figures 22 and 23 present VAS- and LAMPS-derived TB
fields, respectively, for the six comparison times on 6-7
March.  VAS "split window" and LAMPS model clouds are denoted
by scallops.  A cursory examination shows that the model has
captured many of the observed image features.  Good
correspondence between LAMPS and VAS derived cloudy areas is
evident from 1800 GMT through the end of the study period.

The VAS image contours at 1100 GMT (Fig. 22) indicate one
region of relatively warm TBs greater than 242 K over western
Texas, and two others over Oklahoma and Kansas.  Moore and
Fuelberg (1988) tracked the feature over western Texas
upstream to Washington state on 5 March, while the features
over Oklahoma and Kansas were found to develop in situ.
Following Moore and Fuelberg, these will be termed the
"advective" and "development" features, respectively.
Cloudiness dominating the southeastern portion of the region
is responsible for the low TBs.

By 1730 GMT (Fig. 22), the observed warm feature over
western Texas has propagated eastward, intensified to over 246
K, and begun to merge with the TB maximum over southeastern
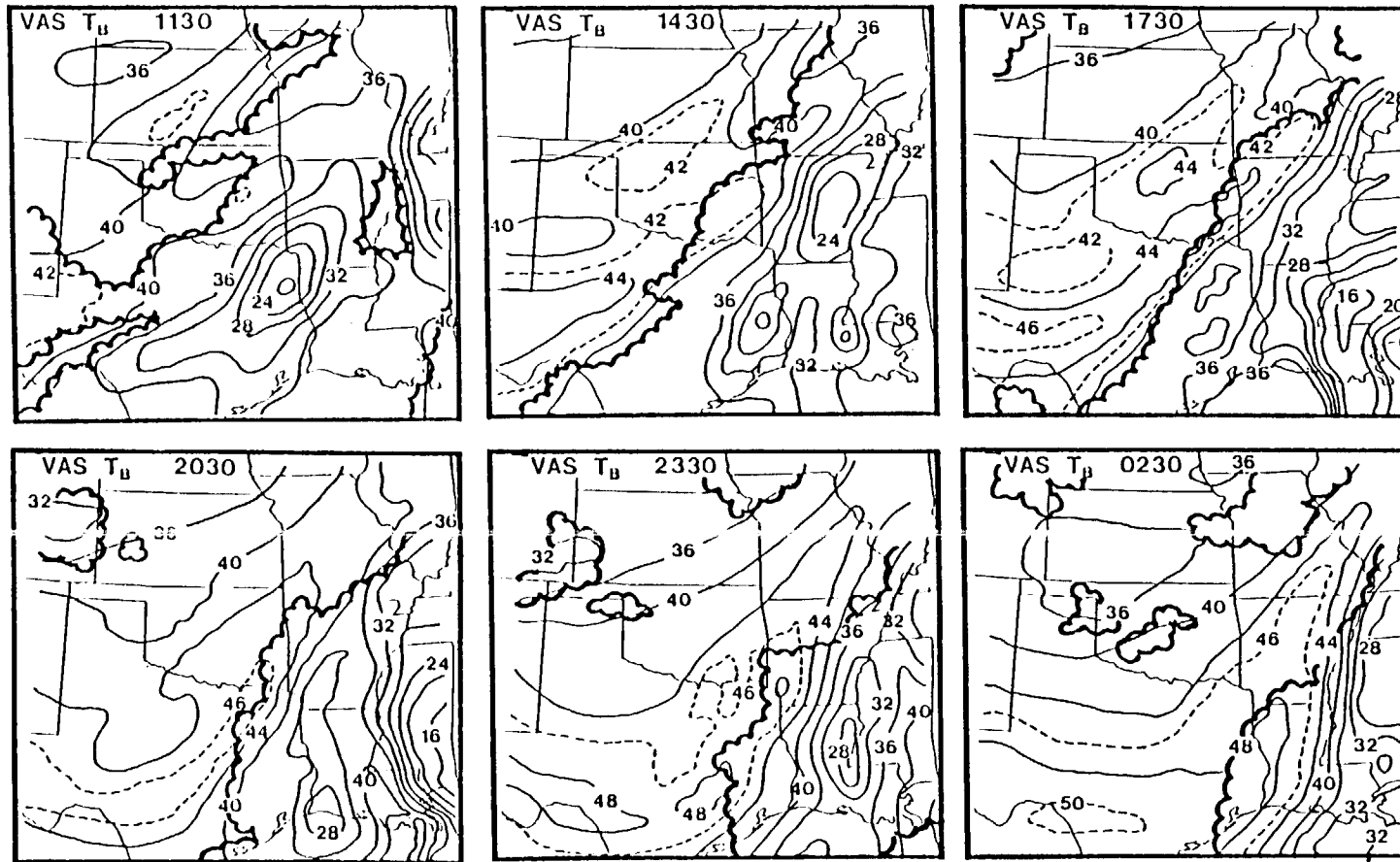
Fig. 22. VAS TB (Kelvins-200, i.e., 36 denotes 236 K) cor-
responding to the water vapor images. Solid contours
are at 4 K intervals while dashed lines indicate
selected intermediate contours at 2 K intervals.
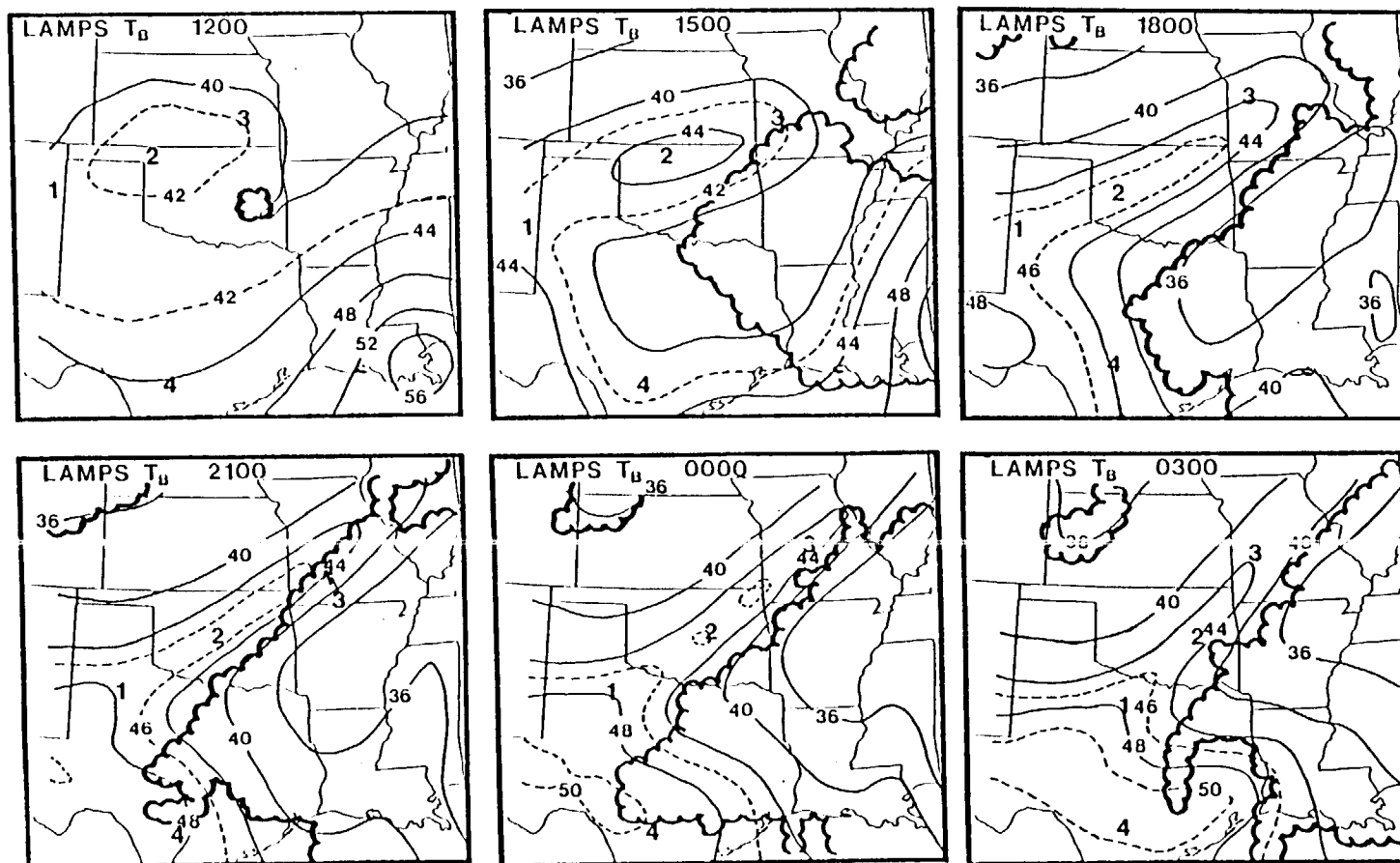Areas within scallops denote VAS "split window" clouds.

Fig. 23. LAMPS TB where areas within scallops denote model cloud water above 750 mb. Otherwise, as in Fig. 22.

Oklahoma. The second component of the development feature, the warm streak over Kansas, has moved southeastward to central Oklahoma and strengthened to 244 K. The 242 K contour now encompasses all of the dry (warm) features and indicates merging of the developing and advecting areas. The low TBs induced by clouds in the Southeast also have pushed eastward.

Observed TBs at 2030 GMT (Fig. 22) display the continued merging of the warm features and expansion of the 244 K and 246 K contours. By 2330 GMT, maximum TBs have increased to 248 K, and the developing portion has merged with the warm region propagating from the west. This advective portion now encompasses most of Texas, while the development section, with its northern end apparently anchored over Missouri and Illinois, is rotating counterclockwise, in phase with the eastward movement of the advective feature. Finally, by 0230 GMT, the last study time, maximum TBs have increased to 250 K, with warm values now extending into Louisiana. The axis of maximum TB extends across southern Texas, then curves northeastward through Louisiana, Arkansas, Missouri, and Illinois.

LAMPS-derived TB patterns (Fig. 23) show many of the evolutionary features seen in the observed VAS water vapor images (Fig. 22), but there also are some important differences. TBs in the cloud free regions compare well, with differences generally ranging from zero to 4 K. Early in the study period, differences are mostly due to model spinup. For example, observed clouds at 1100 GMT (Fig. 22) cover approximately two thirds of the comparison domain, but at 1200 GMT (Fig. 23), the model has only a small patch of clouds. In fact, it is not until comparison period three, i.e., 1800 GMT, that the model yields realistic cloud coverage. This delay is probably attributable to the unsaturated and nearly non-divergent initial state (Kalb, 1987).

Another feature of interest at the first time (Fig. 23) is the extremely warm simulated TB region located over southeast Louisiana. Soundings at 1100 GMT reveal a discrepancy between modeled grid point humidity and that in the observed Bootheville profile. This apparently was due to an error in the initial analysis which combined an observed moisture field with an LFM first guess field. The moisture field contained a spurious dry area in the middle and upper levels, resulting in excessively warm simulated TBs. On the other hand, even if the Bootheville sounding had been accurately reflected in the model, the calculated TBs still would have shown dry middle tropospheric air overlying moist, nearly saturated conditions at the surface. This middle level dryness was not detected by VAS (Fig. 22) due to cloudiness. It also is possible that water vapor was present at altitudes higher than the rawinsonde's detection ability, usually approximately 300 mb. Whatever the cause, it is precisely in this region of convective instability that strong thunderstorms occurred. Since the anomalous TBs are located

52

in the southeastern sector of the study area and quickly move eastward, they are not important to the forecast of the region of greatest interest.

An important measure of a model is its ability to simulate the time evolution of observed features. Examination of the LAMPS TB forecast (Fig. 23) shows that the model had both success and difficulties with this aspect. Specifically, LAMPS locates the advective warm streak over western Texas at 1500 GMT, but does not reproduce its narrow shape seen in the observed image (Fig. 22). Also, the incipient development feature in the simulated TB field at 1200 GMT is delineated by the 242 K contour over the Kansas/Oklahoma border. By 1500 GMT, this structure has elongated, narrowed and intensified. Although its location is coincident with the northern lobe of the observed development feature, the model is not able to simulate the developing portion observed over southeast Oklahoma. This may be attributable to the fact that the observed double structure was not present in the initial model moisture field. Indeed, previous work (Moore and Fuelberg, 1988; Stewart and Fuelberg, 1986) indicates that no such moisture configuration was resolved by the special mesoscale rawinsonde network operating during the study. This illustrates the point that satellites can delineate structures not detected by conventional data.

At 1800 GMT (Fig. 23), the LAMPS developing streak has a maximum TB contour of 246 K, compared with 244 K in VAS (Fig. 22). The advective portion displays a maximum of 248 K as it continues to intensify and propagate eastward over Texas. This compares with 246 K observed by VAS. LAMPS produces a large area of cold TBs over eastern Texas, Arkansas, Louisiana and Mississippi, which in both LAMPS and VAS correspond to cloudy regions. Since the radiative transfer code does not treat LAMPS clouds explicitly, however, simulated TBs in the region are as much as 22 K too warm. A more realistic treatment of clouds by the radiative transfer algorithm would yield more appropriate TBs. Of course, TB in cloudy regions is an unreliable indicator of atmospheric water vapor content.

By 2100 GMT (Fig. 23), the axis of the model development band shifts southeastward similar to that of the VAS image streak (Fig. 22). The former extends from southwest Oklahoma to central Illinois, while the latter is across southeast Oklahoma. The displacement reflects a phase error between the LAMPS and observed upper tropospheric trough locations, probably resulting from the fixed boundary conditions (Kalb et al., 1987). This produces an area of relatively large TB differences over the Texas/Oklahoma border where VAS TBs are warmer than those modeled. Despite the magnitude difference, however, the axis of maximum TBs in both the model and observed cases is associated with the upper level trough. Figure 24 presents simulated absolute vorticity patterns at 500 mb for three times. Two facts are evident; first, both the advective and development image streaks occur in areas of
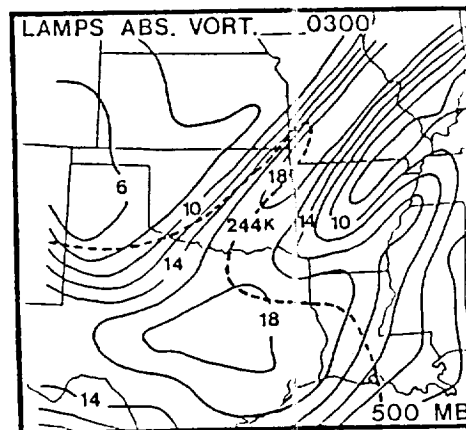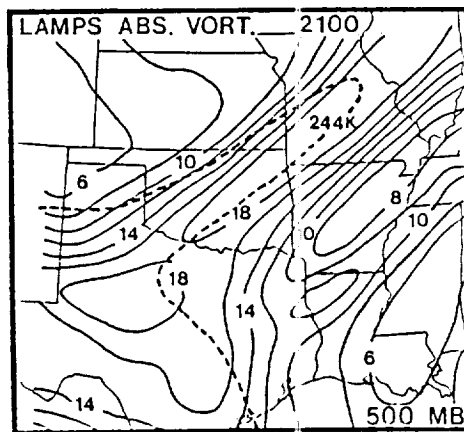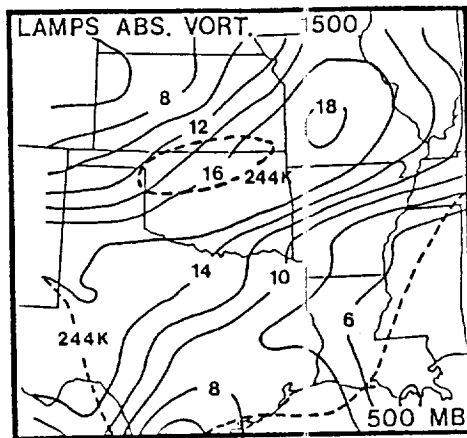
Fig. 24. LAMPS 500 mb absolute vorticity ($\times 10^{-5}$ $s^{-1}$) for times indicated. Dashed line denotes 244 K TB contour.

54

high absolute vorticity, and second, they are primarily in the wake of the vorticity maxima, in areas of negative vorticity advection. Quasi-geostrophic theory suggests that such areas are expected to contain subsidence. Processes by which the leading edges of the dry streaks can move ahead of the axis of maximum vorticity will be examined in a later section using trajectories.

At 0000 GMT, the LAMPS development feature (Fig. 23) appears to be weakening while the observed warm streak (Fig. 22) continues to intensify. This weakening is somewhat of an illusion, however, because examination of unsmoothed TBs (not shown) reveals that the model has narrowed the development feature to the width of a single grid point, and along this narrow axis, the TBs are not significantly decreasing. Unfortunately, any fluctuations along the axis are removed in the smoothing process. Thus, from a large scale perspective, the strength of the model development feature is diminishing, even though at the grid scale its behavior is closer to that observed. The unsmoothed values suggest that significant grid scale weakening of the model development feature does not begin until after 0000 GMT. Final points about the LAMPS 0000 GMT patterns are that the advective portion now covers a substantial fraction of Texas, and the cloudy area has continued to move eastward, ahead of the shortwave trough.

By the final comparison time of 0300 GMT (Fig. 23), the leading edge of the LAMPS advective feature has pushed into Louisiana. Maximum TBs are greater than 250 K over Texas. This aspect of the simulation shows remarkable agreement with its VAS counterpart (Fig. 22). Meanwhile, the phase error of the development streak has increased, with the LAMPS warm band extending from central Oklahoma to northeastern Missouri, while the observed version stretches from eastern Texas to southeastern Missouri. Once again, this displacement is due to the discrepancy between locations of the modeled and observed upper level shortwave trough.

In summary, LAMPS was reasonably successful in depicting observed image structures. Therefore, model output will be used to infer causes for specific image features. In the next section, kinematic parameters associated with the simulated TB fields will be explored.

## 2. Relations Between LAMPS TB and Kinematic Parameters

As a first step toward understanding atmospheric processes responsible for water vapor imagery, LAMPS instantaneous vertical velocity and mixing ratio at 500 mb are examined at 1500, 2100, and 0300 GMT (Fig. 25). Before proceeding, however, several facets of using modeled data
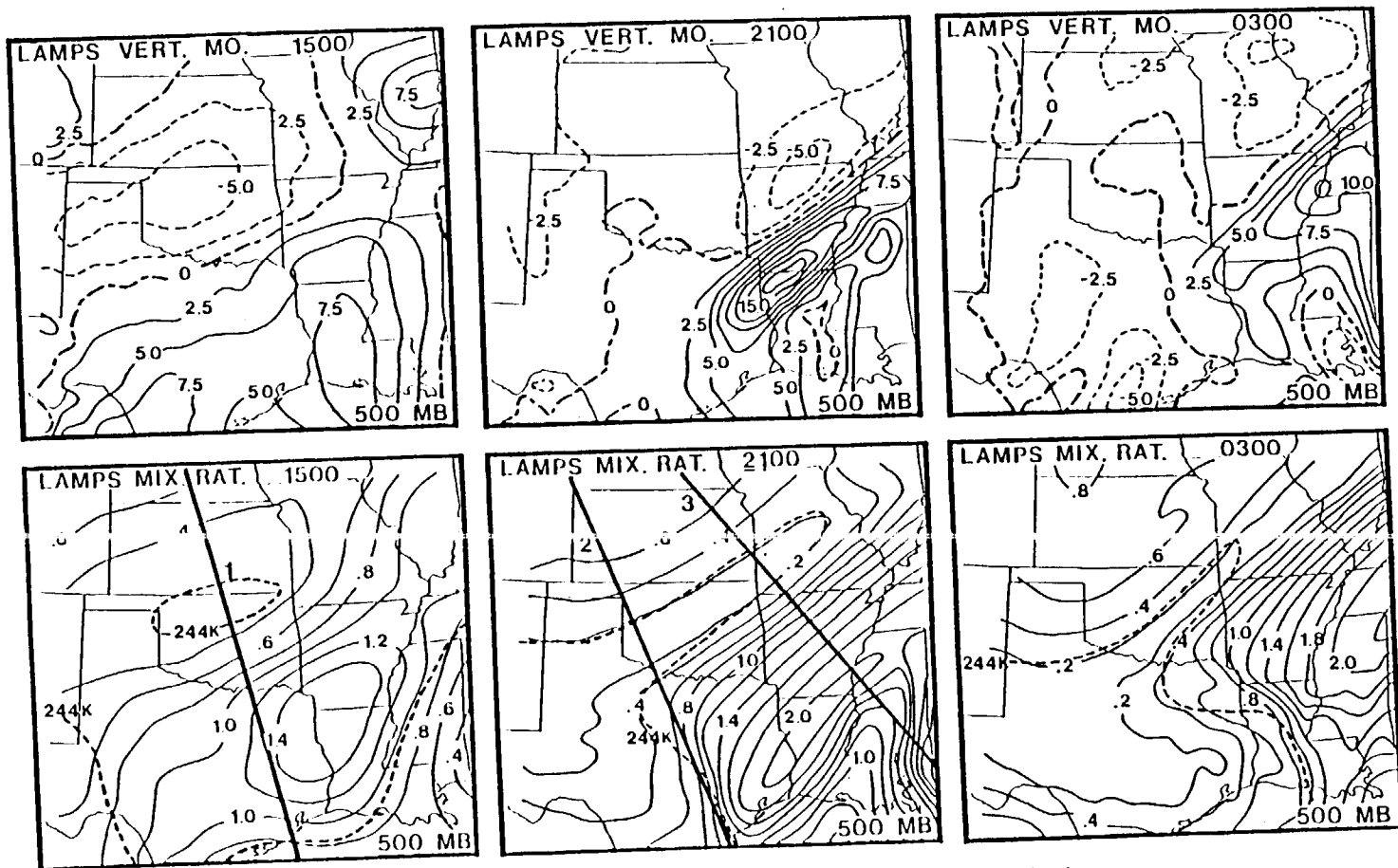
55

Fig. 25. LAMPS 500 mb vertical velocity (cm/s) and mixing
ratio (g/kg) for times indicated. For vertical
velocity, dashed lines indicate negative values and
dash-dot denotes the zero value. Straight solid lines
on mixing ratio plots indicate cross section locations.
Dashed line represents 244 K TB contour.

should be mentioned. Although TB represents integration over many layers of the atmosphere, lack of vertical resolution makes any single model level contribute more than it would in the real atmosphere. In addition, there initially is no moisture at upper model levels due to limitations of the initial RAOB soundings. This means that model TB fields may reflect moisture conditions at lower levels more than would TB in the real atmosphere. Model processes eventually result in moisture being transported to the top levels if there is upward vertical motion, but in areas of subsidence, only horizontal advection can bring water vapor to these levels. As a result of these considerations, the remarkable similarity between LAMPS 500 mb water vapor patterns and simulated TBs (Fig. 23) will not generally occur with observed data.

The mixing ratio patterns (Fig. 25) illustrate the evolution of a broad area of dryness into a narrow zone and give an indirect indication of deformation in airstreams poleward of the shortwave. The LAMPS mixing ratio analysis at 1500 GMT depicts a large area of values less than 0.4 g/kg over Oklahoma, Kansas, and the Texas Panhandle in conjunction with the warm development TB feature (Fig. 23). Vertical motions (Fig. 25) indicate a downward maximum of -6 cm/s coincident with the area of maximum TB and minimum humidity. In general, subsidence is occurring behind the upper level trough (not shown) while the cloudy southeastern portion of the comparison domain is dominated by strong ascent. Thus, the vertical motions inferred from the vorticity analysis (Fig. 24) are indeed reasonable for this case.

During the incipient stages of streak development, it appears that differential vertical motion (Fig. 25) forms the initial moisture gradients and acts to deepen the upper level dry layer. That is, the middle tropospheric subsidence is depressing moisture values in the general region of the warm TBs constituting the development feature.

By 2100 GMT (Fig. 25), it obvious that dark (warm) TB areas (Fig. 23) do not necessarily imply the existence of subsidence at a given instant. This finding is counter to the commonly stated notions about water vapor imagery (e.g., Petersen et al., 1984; Velden, 1987; Monk and Bader, 1988). Specifically, a region of weak ascent has formed in southwest Oklahoma near the junction of the development and advective features, while subsidence greater than -5 cm/s is found southeast of the development streak straddling the 236 K TB contour. The cause of the subsidence southeast of the trough axis over northern Arkansas is not clear. It may be related to the model convection occurring just to its south; alternatively, it may be associated with fluctuations in the jet streak over the Ohio River Valley.

Although vertical velocity patterns at 2100 GMT (Fig. 25) do not suggest the banded shape of the model image feature (Fig. 23), they are consistent with modeling results of Durran

and Weber (1988). Specifically, they found that differential vertical motions initially acted to create moisture gradients, but the subsequent structure of their simulated vertical velocity fields was very different from that of the model cirrus cloud boundary. They showed that broad scale lifting of the previously formed moisture gradient was responsible for the sharp edge of the jet stream cloud shield. Thus, current results about subsidence appear to be the water vapor imagery equivalent of their findings.

Differences between areas of subsidence and warm TB also are evident in Fig. 26, which contains a cross section of vertical velocity, mixing ratio, and TB at 2100 GMT. The placement is the westernmost axis shown in Fig. 25. The cross section, passing through the southwestern part of the elongated image feature, reveals that the weak ascent within the dry streak extends only below 500 mb. It also shows, however, that even above this level, where vertical motions might be expected to more strongly affect the TB field, the maximum subsidence is found far north of the dry development streak. Maximum TB is just south of the lowest dip in the 0.5 g/kg mixing ratio isopleth, probably due to the minimum in the moisture field above this level as seen in the shape of the zero isopleth.

Vertical velocity patterns over Texas at 2100 GMT (Fig. 25) reveal that the leading edge of the advecting dark (warm) area (Fig. 23) actually extends eastward into the retreating region of ascent. This suggests that air which may have originally derived its dryness through subsidence is being advected horizontally into regions of rising motion. This provides further evidence that water vapor images do not represent the instantaneous pattern of vertical velocity, but rather the manifestation of the history of air motions.

The narrowness and intensification of the dry region at 2100 GMT (Fig. 25) corresponds to the upper level frontogenesis described by Moore and Fuelberg (1988). Furthermore, this scenario agrees with findings about upper level frontogenesis presented in Bosart (1970), Keyser and Shapiro (1986) and others. Specifically, the 6-7 March period begins as the shortwave (Fig. 14) has almost passed through the major trough. Bosart (1970) noted that this stage of upper level frontal development is characterized by confluent horizontal processes, and by thermally direct vertical circulations, which in the current case are seen in Figs. 25 and 26. While these vertical motions initially result in development of the simulated dry image streak over Oklahoma, it is the deformation and wind shears associated with the model shortwave that cause the narrowing manifested in the 500 mb LAMPS mixing ratios. These will become clearer in the next section when model trajectories are presented.

It is tempting to attribute the weakening of the LAMPS development feature at 0300 GMT (Fig. 23) to the ascent over
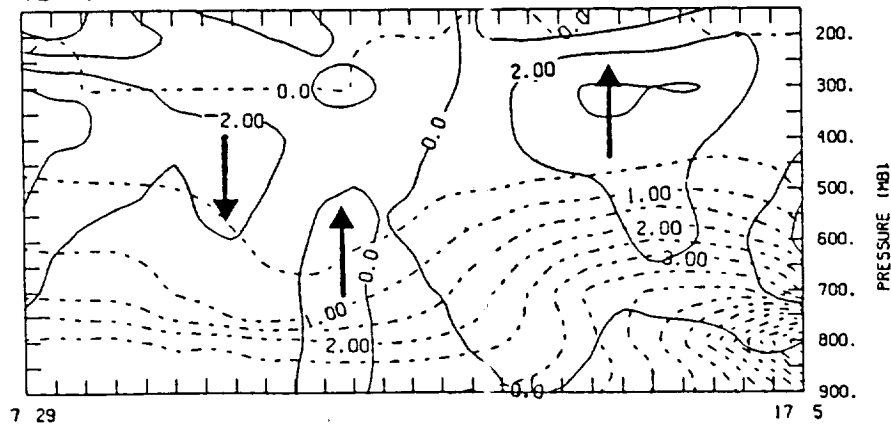
BRIGHTNESS TEMP. (K)          21Z   06 MAR 82
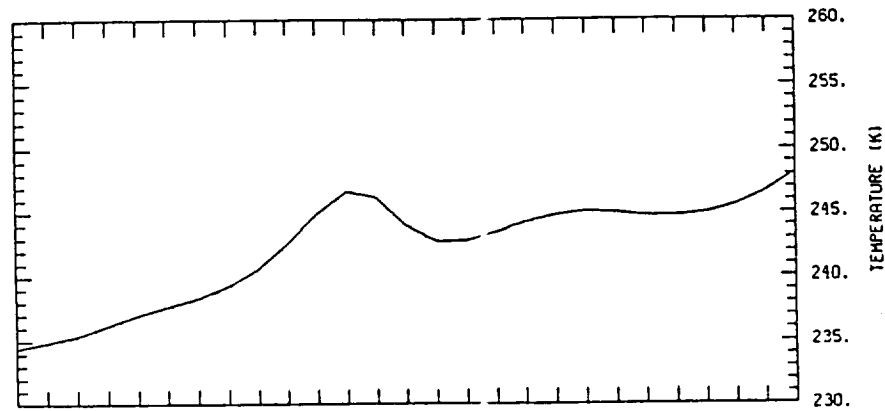
VERT. MØ. (CM/S)/ MXRAT. (G/KG)   21Z   06 MAR 82

LAMPS X-SECTIØN

Fig. 26. Cross section of LAMPS vertical velocity (solid, contours
every 2.0 cm/s) and mixing ratio (dashed, contours every
0.5 g/kg). Location for cross section is the
westernmost axis in Fig. 25 at 2100 GMT. LAMPS TB (Kelvins)
along the cross section is plotted above.

Oklahoma at 500 mb (Fig. 25). However, close examination reveals that TBs near southern Missouri and northern Arkansas also have decreased by an equal amount even though they are located in a region of -5 cm/s descent! In fact, trajectory results in the next section will show that once the strong moisture gradients have formed during the early stages of streak development, it is the origin of air parcels with respect to the gradients that controls whether or not TBs continue to increase. The simulated dry band (Fig. 23) over Oklahoma and Missouri corresponding to the development feature continues to narrow while the moisture gradient southeast of this system intensifies.

Regarding the advective image feature at 0300 GMT (Fig. 23), its leading edge has moved to Louisiana, where there is ascent greater than 2.5 cm/s. Again, it appears that this is a manifestation of dry air being brought down from upper levels at distant sites, then being horizontally advected ahead of the vorticity maximum.

## 3. LAMPS Trajectory Analyses

Parcel trajectories were computed from the LAMPS three hourly model output to gain additional insight into processes associated with the warm (dry) streaks in water vapor imagery. Figure 27 reveals basic characteristics of upper tropospheric airstreams based on trajectories ending at 400 mb at 0300 GMT. The trajectories are superimposed on the 244 K TB contour delineating the image bands. Parcels northwest of the streak, behind the shortwave trough, are moving southward and descending. For example, between 1500 to 0300 GMT, parcels 1 and 2 experience subsidence of 43 and 35 mb, respectively. On the other hand, parcels 6 and 7 ending east of the development feature are moving much faster and ascending in the southwesterly jet flow ahead of the shortwave. They rise 15 and 46 mb respectively, during the period 1500 to 0300 GMT. The opposing flow patterns depicted by the trajectories provide evidence of the confluence and wind shears associated with the dry streak and shortwave within the major trough.

Parcel 4 (Fig. 27) lies directly within the dry development band. It subsides 34 mb between 1200 to 0300 GMT, but 27 mb of that amount occurs during the first 6 h of the study period, while only 7 mb occurs during the final 9 h of the parcel's journey. Tracing its path back through time, it is obvious that this parcel is moving separately from those on either side of the development image. In fact, its location at each time is coincident with the model warm TB area (Fig. 23). Thus, it appears that the parcel is "trapped" within the slowly moving air accompanying the shortwave trough. Its behavior is consistent with the hypothesis that strong
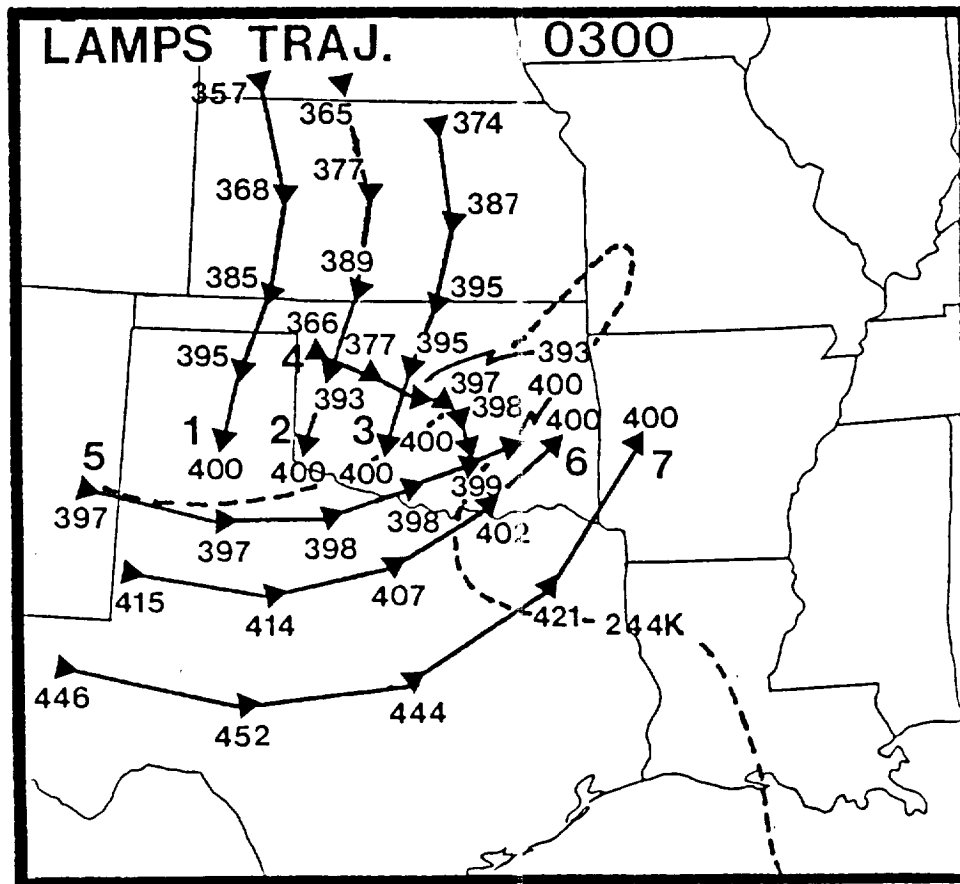
60

Fig. 27. LAMPS trajectories ending at 0300 GMT 7 March and
400 mb computed over three hour increments. The
dashed line indicates the 244 K LAMPS TB contour.

subsidence near the beginning of the period results in the dryness characterizing the warm image feature, but that strong sinking is not present throughout the life histories of the parcels comprising the streak.

Backward trajectories that end at the 465 mb sigma-height model level at 2100 GMT are shown in Fig. 28. This is the period during which the model development feature intensifies the most. An interesting aspect of trajectories 1, 2, and 3 that end within the development streak is that each can be traced back to a location within the initial warm TB feature at 1200 GMT (Fig. 23). This agreement lends credibility to the trajectory calculations. In fact, a close examination of parcel locations reveals that they are near the axis of maximum TB at all times prior to 2100 GMT. This means that the core of the development feature is moving with the parcels. Points 1 and 2 are traveling from northerly and northwesterly directions, respectively, while point 3 comes from the southwest, thus affecting the deformation of the dry pattern. All three originated at approximately 415 mb, undergoing nearly 50 mb of subsidence. The path from point 1 is almost normal to the development feature, while that from point 3 is almost parallel with the warm TB core. This causes the base of the image feature to move more than its northern end, resulting in the previously mentioned counterclockwise rotation. The water vapor content of these parcels is small, ranging from 0.02 to 0.04 g/kg. Parcel 5, ending northwest of the development band, can be traced to 1500 GMT before leaving the model domain. However, between this time and 2100 GMT, it subsides only 19 mb, compared with 36 to 38 mb during the same period for parcels 1-3 ending within the dry streak. More importantly, it contains 0.3 g/kg of water vapor, or nearly an order of magnitude more than parcels in the dry band. Southeast of the development feature, parcel 6 ascends nearly 90 mb in the southwesterly flow ahead of the shortwave between 1200 and 2100 GMT. This parcel is located within the model cloudy region and ends with a mixing ratio of 0.85 g/kg at the 469 mb level.

The important points describing evolution of the development feature can be summarized. It appears that the total amount of subsidence that a parcel undergoes is not related to the TB at its final destination. Localized strong subsidence is an important factor in establishing the pronounced moisture gradients, but overall weak subsidence within and outside of the streak then acts to maintain these gradients. Parcels within the band may even experience ascent at times during their histories, but because of their dry origins, the satellite sensor will still "see" through the deep dry layer to the moister, warmer air in the middle troposphere. All the while, the horizontal deformation of the northwesterly airstream poleward of the upper level shortwave helps to shape and transport the dry band.
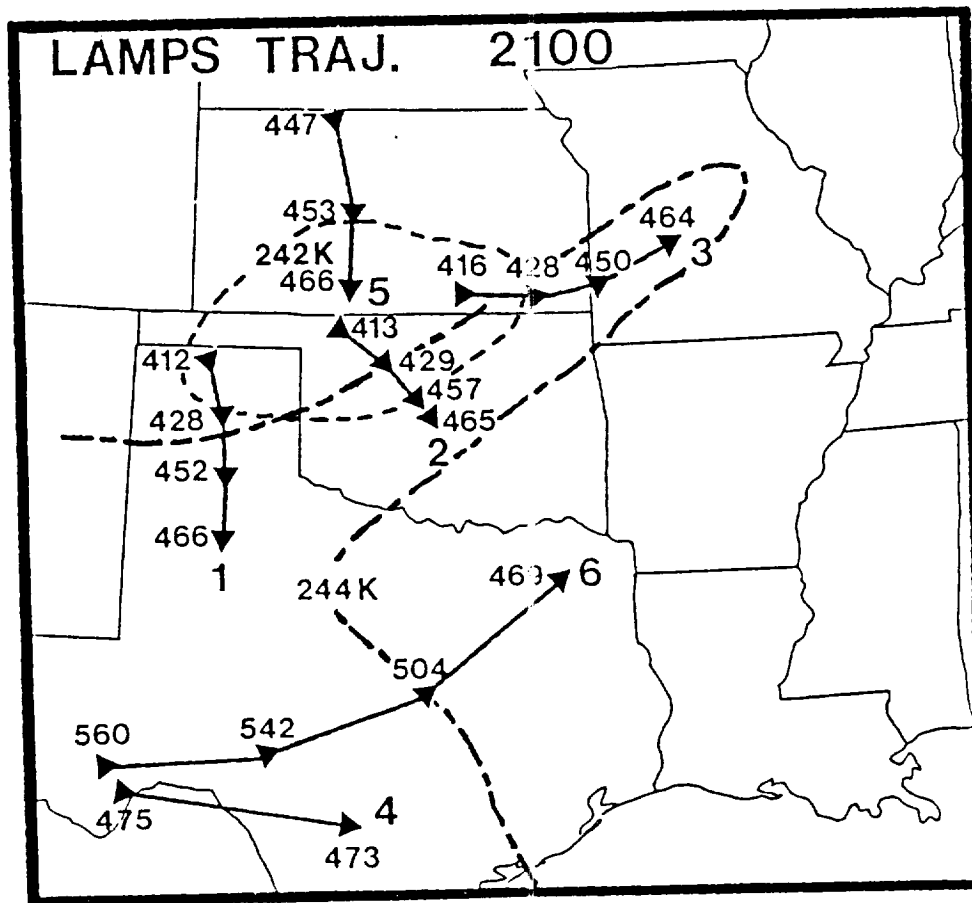
Fig. 28. Same as Fig. 27 but for 2100 GMT 6 March and approx-
imately 465 mb. The dashed line indicates the 242 K
TB contour for 1200 GMT and dash-dot indicates the
244 K TB contour for 2100 GMT.

A backward trajectory from point 4 (Fig. 28), chosen for its location within the advective streak, can be traced back only to 1800 GMT due to the strong jet flow in the region. Although it is associated with TB greater than 248 K at 2100 GMT, the parcel actually ascends 2 mb in the 3 h period. This trajectory appears to corroborate the findings of Rodgers et al. (1976) that some of the dry patterns seen in water vapor images are the result of horizontal transport of previously subsided dry air. In other words, warm TBs can occur in regions of upward motion if the air is sufficiently dry.

## 4. Sonde-Derived Trajectories

Attention now will focus on trajectories made from the 3 hourly rawinsonde data as a verification of the modeling results. The general behavior of airstreams is given by estimated parcel paths computed backward from 0245 GMT and 400 mb, labeled 1-7 from left to right in Fig. 29. In general, sonde-derived trajectories display good qualitative similarity with those from LAMPS (Fig. 27). Specifically, parcels ending west of the TB streak come from a northerly direction and experience strong subsidence, while those to the east ascend in the southwesterly jet flow ahead of the upper level trough. The sonde-derived trajectories generally depict greater change in altitude than those from LAMPS due to stronger vertical motions from the sonde data (not shown). Trajectory 4 is similar to that of LAMPS parcel 4 (Fig. 27) in that its path can be traced backward within the developing dry band to the warm TB axis over the Oklahoma Panhandle at 1100 GMT (Fig. 22). It is the slowest moving of all seven parcels, sinking 50 mb in the 9 h from 1745 to 0245 GMT, compared with approximately 75 mb in the same period for parcels 1-3. A comparison with Moore and Fuelberg (1988) suggests that parcel 4 was within the upper portion of a sloping stratospheric extrusion, or tropopause fold. Parcel 5 also appears to have been within the tropopause fold. In contrast to parcel 4, however, it is moving rapidly in the westerly flow, and can be traced back to the leading edge of the advective streak in southwestern New Mexico (not shown in plot) at 1100 GMT, having descended 50 mb during its journey. Parcel 6 sinks 39 mb during the 3 h from 1445 to 1745 GMT, then ascends 29 mb from 1745 to 0245 GMT, maintaining a position near the southeastern edge of the warm TB band. These displacements are similar to those observed from model data, i.e., suggesting that parcels may sink in the wake of the vorticity maximum, but then move through it in the jet flow, and ascend as they move along the leading edge of the image streak.

One cause for differences in the evolution of the model and observed warm features is revealed by differences in model- (Fig. 27) and sonde-derived (Fig. 29) trajectories ending at 400 mb. Specifically, parcel 6 in Fig. 29 shows
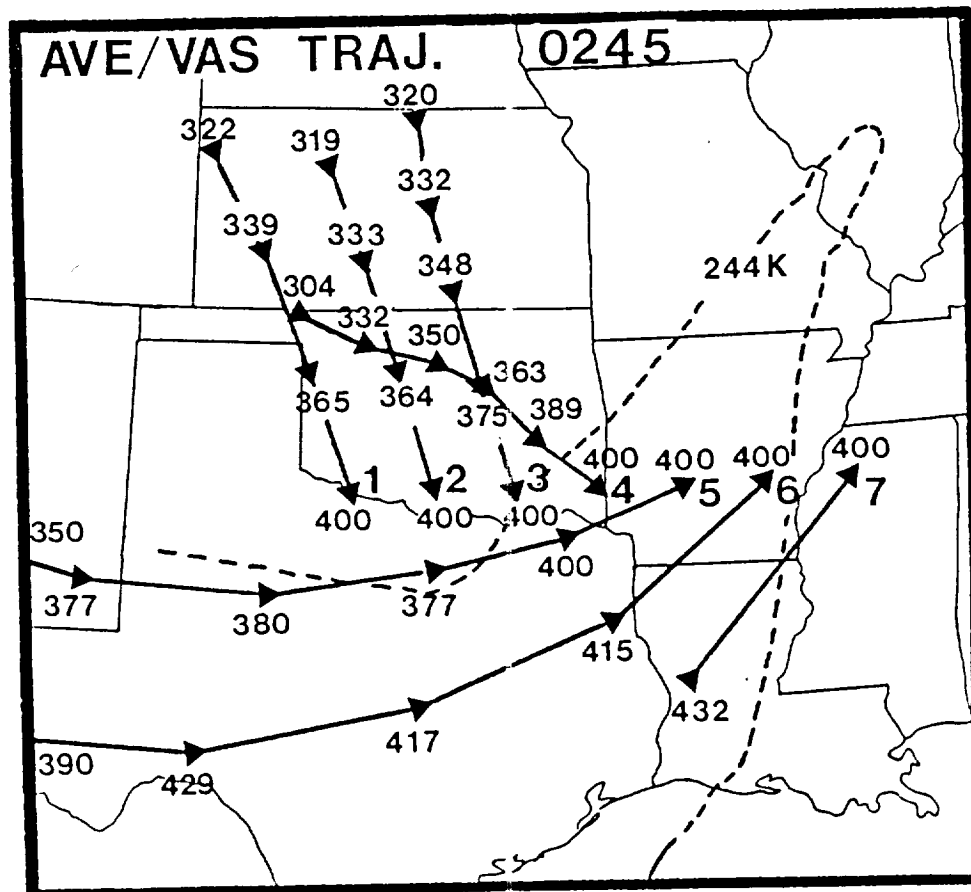
64

Fig. 29. RAOB trajectories ending at 0245 GMT 7 March and 400 mb computed for time increments corresponding to the RAOB times. The dashed line indicates the 244 K TB contour for 0230 GMT.

that air accompanying the observed advective streak travels in
a curved path, ultimately turning to the northeast and moving
into the development portion of the streak. This apparently
facilitates the merger with the development portion that is
observed in the imagery (Fig. 22). With LAMPS, however, the
advective and development features are not in phase, and
parcels moving in the southeastern part of the advective
feature advance more nearly eastward. Unlike their RAOB
counterparts, parcels ending near the core of the LAMPS
development feature over Oklahoma (Fig. 27) appear to be
associated with the northwesterly flow and the incipient
development feature. Thus, if the model had phased the two
streaks as actually observed, TBs in the development band
might have continued to increase as they did in the advective
feature.

Turning now to parcels specifically representing the
image streaks, Fig. 30 shows four trajectories ending in the
development or advective portions at 2045 GMT, along with two
others at different locations. These trajectories were
computed backward from the 465 mb level to facilitate
comparison with LAMPS versions shown previously (Fig. 28).
There are both qualitative similarities and differences
between the two versions. For example, RAOB parcels 2 and 3
move with the development feature, although their directions
are more westerly than those from LAMPS. During the period
1100 to 2045 GMT, these parcels subside 88 and 53 mb,
respectively, compared with approximately 50 mb for LAMPS
parcels in similar relative positions.

Comparing trajectories within the TB feature with one
ending northwest of the development streak (Fig. 30) shows
that parcels 2 and 3 subside 49 and 63 mb, respectively,
between 1445 and 2045 GMT, while parcel 5 sinks a similar 45
mb. Thus, the role of differential subsidence early in streak
development is more evident in the model case. Like the LAMPS
versions, sonde-derived paths well behind the trough (parcel
5) are northerly.

In contrast to points 2 and 3, parcels 1 and 4, located
further south (Fig. 30), are within the jet flow accompanying
the advective streak. Each parcel stays within the warm TB
boundaries (Fig. 22) during its movement eastward, and each
ascends and descends during passage through the computational
domain. Parcel 6, meanwhile, reflects the strong
southwesterly ascent into the stormy region over the Gulf
Coast, rising 138 mb in 6 h.

In summary, the LAMPS model yields results qualitatively
similar to those calculated from RAOB data. Phase
differences, discrepancies in vertical motion fields,
differences in the initial moisture field, and lack of
vertical resolution with the model explain some of the
contrasting results in the two data types. However, the fact
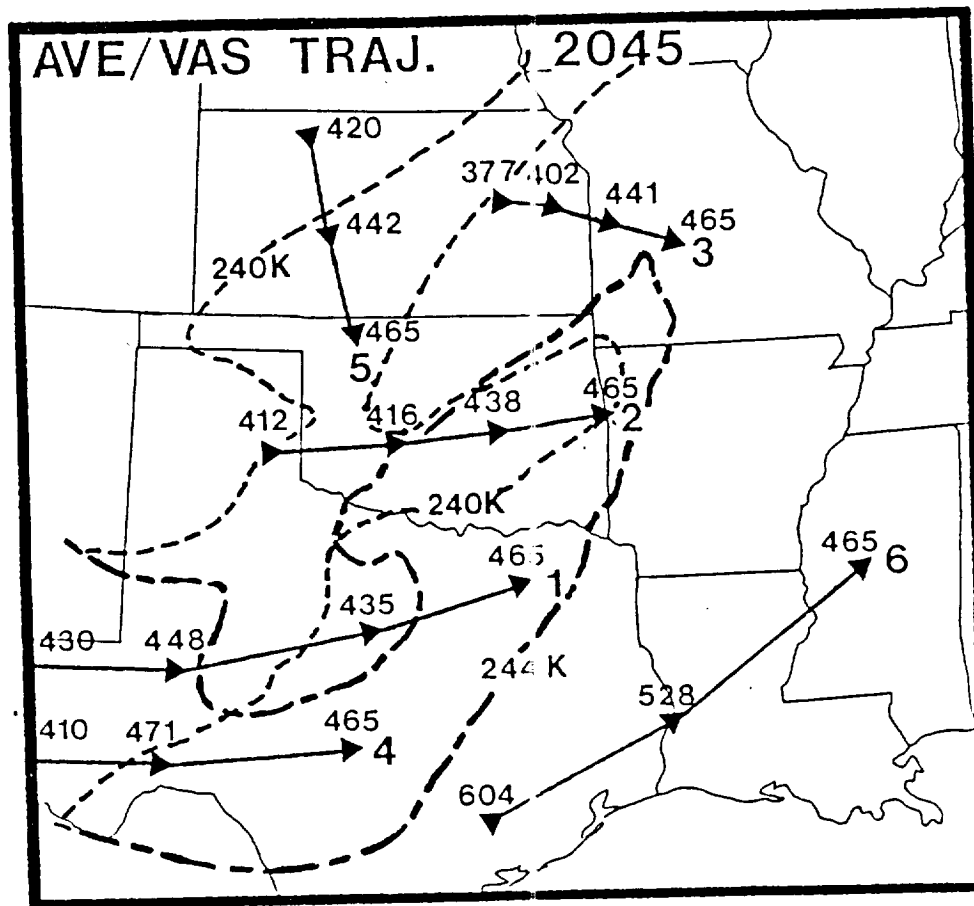that the model was able to capture many aspects of the dry

Fig. 30. As in Fig. 29 but for 2045 GMT 6 March and 465 mb.
Dashed lines indicate the 240 K TB contour for
1100 GMT and dash-dot indicates the 244 K TB contour
for 2030 GMT.

streaks, combined with self-consistency of model TBs and dynamics allow simulated and observed findings to be synthesized into a conceptual model of image streaks.

# D. CONCLUSIONS

Comparison of model generated and observed TBs showed that LAMPS captured major features of the VAS imagery, including the pronounced dry "development" streak, and a cold cloud area. The model-derived depiction of the "advective" image feature also was quite good. On the other hand, the model did not resolve some finer scale details such as the double structure of the development streak. This may result from the inability of the initial moisture analysis to resolve this small feature. Although LAMPS reproduced several evolutionary aspects of both portions of the image streak, including the intensification and eastward propagation of the advective component over Texas and the rotation of the development feature, it did not duplicate the observed continuous strengthening of the development portion.

With three hourly radiosonde-derived products and VAS images as verification, LAMPS output was a valuable tool for explaining causes for the image configurations. Model trajectories associated with the simulated imagery showed good qualitative agreement with those calculated from radiosonde data. Based on a synthesis of model and observed information, the following conclusions can be made concerning atmospheric processes associated with the warm TB image streaks.

The development feature formed along the axis of the upper level shortwave trough as it moved through the major trough. The image feature formed within the negative vorticity advection and associated subsidence behind the trough line. Both modeled and observed moisture gradients at the beginning of the study period were enhanced by strong differential subsidence within the first 6 h of the investigation. This acted to intensify the development image feature. Horizontal confluence associated with the strong wind shears accompanying the upper level shortwave and jet stream caused the dry feature to elongate along the trough line. The development feature appears to be consistent with Bosart's (1970) depiction of upper level frontogenesis during the latter stages of a disturbance moving through a major trough. Specifically, upper level development during this period was characterized by confluent horizontal processes, while vertical circulations were thermally direct.

Once the strong downward velocities had formed the dry streak, horizontal transport played a major role in producing upper tropospheric variability experienced at given locations.

68

At this stage in the evolution, TB patterns could not be equated to a "snapshot" of the vertical velocity fields, because dry air that had originally subsided could now be moving horizontally or even rising. Trajectories showed that air near the leading edge of the development feature was often ascending, thereby helping explain the observation (Petersen et al., 1984) that thunderstorms often form near the edges of dry image bands when they move over regions of low level moisture.

Model results revealed that the advective feature also was associated with an upper level vorticity maximum. This maximum resulted from speed shear accompanying the propagation of a polar jet streak around the major trough. Because air within this warm band was traveling faster than the vorticity field itself, parcels appeared to sink in the rear of the vorticity maximum, move through it and then rise ahead of it. However, even though rising, they retained their dry characteristics, still appearing as a warm TB feature.

Both model and observed trajectories indicated that flow behind the development feature and north of the advective portion was northerly or northwesterly and generally subsiding. Air streams east and southeast of the image features were generally ascending. In contrast, parcels ending within the development feature remained within the image streak as they were traced backward in time. These parcels were subsiding during much of their path. Thus, they moved separately from the other two air streams and appeared to be within a zone of stratospheric air defining a tropopause fold (Moore and Fuelberg, 1988). The slowly moving air within the development streak advanced at a large angle to the feature, resulting in southeastward propagation. Air within the advective feature, on the other hand, was moving parallel to its orientation, within the jet flow. In the observed case, this resulted in rapid eastward and northeastward movement, and eventual merging with the development feature.

# VI. CONCLUSIONS

Four interrelated investigations have examined the analysis and use of VAS satellite data. The case study of VAS-derived stability parameters on 21 July 1982 suggested that VAS data would have been a useful supplement to conventional data in the forecasting of thunderstorms. For example, patterns and evolutions of LI frequently were associated with either the development or lack of convection, and the LI variations were not simply attributable to changes in surface conditions. Values of positive and negative energy were similarly useful. On the other hand, the meteorological significance of small or short lived stability features is still uncertain. Such features may at times represent important atmospheric conditions, but data uncertainty is also a factor. Our inability to distinguish the two is partly due to our very limited understanding of mesometeorological phenomena, which is attributable to the scarcity of mesoscale data.

A second study examined the roles of the first guess and VAS radiometric data in producing retrievals of temperature and humidity as functions of height (i.e., soundings). It appeared that the radiance data often did not have a decisive influence on the final satellite soundings for this case. In other words, broad-scale patterns and gradients of the first guess, radiances and retrievals often were similar. The retrievals also had small scale details, especially in the dew point fields. Their origin was sometimes uncertain, i.e., it was unclear whether they were a realistic outgrowth of the VAS radiance data or were due to limitations of the retrieval algorithm, cloud contamination, or other factors.

Two research tasks involved 6.7 micron middle tropospheric water vapor imagery on 6-7 March 1982. The first utilized radiosonde data over the entire United States to examine causes for two areas of warm brightness temperature. One area advected across the nation while the other formed locally over the Midwest. The advecting area of warm TBs was associated with descent near the entrance region of a polar jet streak. On the other hand, the developing image feature was coincident with a tropopause fold and associated intrusion of dry stratospheric air into the middle troposphere.

The second task involving 6.7 micron water vapor imagery on 6-7 March 1982 utilized LAMPS mesoscale simulated data as input to radiative transfer code. Thus, numerical simulations of the imagery were obtained. Evolutions of the simulated image patterns generally compared favorably with those observed; however, some of the observed small scale features

70

were not properly portrayed. Trajectory calculations were
especially valuable in understanding causes for image
development. Although subsidence was important in producing
the areas of warm TB, it was found that TB patterns could not
be equated to a "snapshot" of the vertical velocity fields,
because dry air that had originally subsided could now be
moving horizontally or even rising.

In conclusion, VAS retrievals and water vapor imagery are
powerful tools for diagnosing the atmosphere. They are true
mesoscale data sources that can be available on global scales.
However, these data have their own special limitations that
differ from those of the traditionally used radiosondes.
Investigations such as this will enable us to use the data
such that VAS's strengths are utilized while its limitations
are suppressed.

# REFERENCES

Andrews, M. J., 1987: Assessment of VAS-derived products created by a simultaneous algorithm on a convectively active day. Master's Thesis, Florida State University, 109 pp. (Available from Prof. Fuelberg).

Andrews, M. J., and H. E. Fuelberg, 1988: Satellite derived stability parameters during a convective outbreak. Preprints, 15th Conf. Severe Local Storms, Baltimore, Amer. Meteor. Soc., 178-181.

Anthony, R. W., and G. S. Wade, 1983: VAS operational assessment findings for Spring 1982/1983. Preprints, 13th Conf. Severe Local Storms, Tulsa, Amer. Meteor. Soc., J23-J28.

Barnes, S. L., 1973: Mesoscale objective map analysis using weighted time-series observations. NOAA Tech. Memo. ERL NSSL- 62, National Severe Storms Laboratory, Norman, OK 73069, 60 pp. (NTIS COM-73-10781).

Beven, J. L., 1988: Relations between VAS soundings and their first guess input. Master's Thesis, Florida State University, 119 pp. (Available from Prof. Fuelberg).

Beven, J. L., and H. E. Fuelberg, 1988: Relations between VAS physical retrievals and their first guess input. Preprints, Third Conf. Satellite Meteor. and Ocean., Anaheim, Amer. Meteor. Soc., 41-46.

Bosart, L. F., 1970: Mid-tropospheric frontogenesis. Quart. J. Royal Meteor. Soc., 96, 442-471.

Chesters, D., D. A. Keyser, D. E. Larko, and L. W. Uccellini, 1988: Improved VAS regression soundings of mesoscale temperature features observed during the Atmospheric Variability Experiment on 6 March 1982. Preprints, 3rd Conf. Satellite Meteor. and Ocean., Anaheim, Amer. Meteor. Soc., 35-40.

Danielsen, E. F. 1961: Trajectories: Isobaric, isentropic and actual. J. Meteor., 18, 479-486.

_____, 1968: Stratospheric-tropospheric exchange based on radioactivity, ozone, and potential vorticity, J. Atmos. Sci., 25, 502-518.

Durran, D. R., and D. B. Weber, 1988: An investigation of the poleward edges of cirrus clouds associated with mid-latitude jet streams. _Mon. Wea. Rev._, 116, 702-714.

Fuelberg, H. E., and T. W. Funk, 1987: Diagnosis of vertical motion from VAS retrievals. _J. Climate Appl. Meteor._, 26, 1655-1670.

_____, and P. J. Meyer, 1986: An analysis of mesoscale VAS retrievals using statistical structure functions. _J. Climate Appl. Meteor._, 25, 59-76.

Gandin, L. S., 1963: Objective analysis of meteorological fields. Translated from Russian, Israel Program for Scientific Translations, Jerusalem, 242 pp. (NTIS TT-65-50007).

Gidel, L. T., and M. A. Shapiro, 1979: The role of clear air turbulence in the production of potential vorticity in the vicinity of upper tropospheric jet stream-frontal systems. _J. Atmos. Sci._, 36, 2125-2138.

Hales, J. E., Jr., and C. A. Doswell, III, 1982: High resolution diagnosis of instability using hourly surface lifted parcel temperatures. _Preprints, 13th Conf. Severe Local Storms_, San Antonio, Amer. Meteor. Soc., 172-175.

Hayden, C. M., 1988: GOES-VAS simultaneous temperature-moisture retrieval algorithm. _J. Appl. Meteor._, 27, 705-733.

Heckley, W. A., and B. J. Hoskins, 1982: Baroclinic waves and frontogenesis in a non-uniform potential vorticity semi-geostrophic model. _J. Atmos. Sci._, 39, 1999-2015.

Hillger, D. W., and T. H. Vonder Haar, 1979: An analysis of satellite infrared soundings at the mesoscale using statistical structure and correlation functions. _J. Atmos. Sci._, 36, 287-305.

Jedlovec, G. J., 1985: An evaluation and comparison of vertical profile data from the VISSR Atmospheric Sounder (VAS). _J. Atmos. Oceanic Technol._, 2, 559-581.

Kalb, M. W., 1987: The role of convective parameterization in the simulation of a Gulf Coast precipitation system. _Mon. Wea. Rev._, 115, 214-234.

_____, F. Robertson, G. Jedlovec, and D. Perkey, 1987: Use of simulated radiances from a mesoscale numerical model to understand kinematic and dynamic processes. Preprints, 3rd Conf. Mesoscale Processes, Vancouver, Amer. Meteor. Soc., 129-134.

Keyser, D., and M. A. Shapiro, 1986: A review of the structure and dynamics of upper-level frontal zones. Mon. Wea. Rev., 114, 452-499.

_____, and L. W. Uccellini, 1987: Regional models: Emerging research tools for synoptic meteorologists. Bull. Amer. Meteor. Soc., 68, 306-320.

Monk, G. A., and M. J. Bader, 1988: Satellite images showing the development of the storm of 15-16 Oct. 1987. Weather, 43, 130-134.

Moore, S. R., 1987: Case study of processes responsible for observed patterns in 6.7 micron satellite water vapor imagery. Masters Thesis, Florida State University. 93 pp. (Available from Prof. Fuelberg).

Moore, S. R., and H. E. Fuelberg, 1988: Relations between water vapor imagery, vertical motion and tropopause folds. Preprints, 3rd Conf. Satellite Meteor. and Ocean., Amer. Meteor. Soc., Anaheim, 203-208.

Mosher, F. R., and T. Schoeni, 1988: Assessment of the utility of VAS data products for severe local storms forecasting. Preprints, 15th Conf. Severe Local Storms, Baltimore, Amer. Meteor. Soc., 182-185.

Mostek, A., L. W. Uccellini, R. A. Petersen, and D. Chesters, 1986: Assessment of VAS soundings in the analysis of a pre-convective environment. Mon. Wea. Rev., 114, 62-87.

Muller, B. M., 1988: A simulation and diagnostic study of waterg vapor image dry bands. Master's Thesis, Florida State University, 98 pp. (Available from Prof. Fuelberg).

Muller, B. M., and H. E. Fuelberg, 1988: Simulation and diagnosis of water vapor imagery with mesoscale model output. Preprints, 8th Conf. Numerical Wea. Pred., Baltimore, Amer. Meteor. Soc., 301-308.

O'Brien, J. J., 1969: Alternative solutions to the classical vertical velocity problem. J. Appl. Meteor., 9, 197-203.

Perkey, D. J., 1976: A description and preliminary results from a fine-mesh model for forecasting quantitative precipitation. Mon. Wea. Rev., 104, 1513-1526.

Petersen, R. A., J. H. Hohman, and D. A. Keyser, 1984: Advective forecasts of VAS imagery for use in anticipating convective destabilization. Preprints, 10th Conf. Wea. Forecasting and Analysis, Clearwater, Amer. Meteor. Soc., 365-372.

Petterssen S., 1956: Weather Analysis and Forecasting, Vol. 1, New York, McGraw-Hill, 428 pp.

Reiter, E. R., 1972: Atmospheric Transport Processes, Part 3: Hydrodynamic Tracers. U. S. Atomic Energy Commission, 212 pp.

Rodgers, E. B., V. V. Salomonson, and H. L. Kyle, 1976: Upper tropospheric dynamics as reflected in Nimbus 4 THIR 6.7 micron data. J. Geophys. Res., 81, 5749-5758.

Shapiro, M. A., 1970: On the applicability of the geostrophic approximation to upper-level frontal-scale motions. J. Atmos. Sci., 27, 408-420.

Smith, W. L., 1983: The retrieval of atmospheric profiles from VAS geostationary radiance observations. J. Atmos. Sci., 40, 2025-2035.

Staley, D. O., 1960: Evaluation of potential vorticity changes near the tropopause and the related vertical motions, vertical advection of vorticity, and transfer of radioactive debris from stratosphere to troposphere. J. Meteor., 17, 591-620.

Stewart, M. R., and H. E. Fuelberg, 1986: Relationships between 6.7 micrometer imagery and radiosonde derived parameters. Preprints, 2nd Conf. Satellite Meteor. /Remote Sensing and Appl., Williamsburg, Amer. Meteor. Soc., 67-72.

Uccellini, L. W., D. Keyser, K. F. Brill, and C. H. Wash, 1985: The Presidents' Day cyclone of 18-19 February 1979: Influence of upstream trough amplification and associated tropopause folding on rapid cyclogenesis. Mon. Wea. Rev., 113, 962-988.

Velden, C. S., 1987: Satellite observations of Hurricane Elena (1985) using the VAS 6.7 micron "water-vapor" channel. Bull. Amer. Soc., 68, 210-215.

Weinreb, M. P., and M. L. Hill, 1980: Calculation of atmospheric radiances and brightness temperatures in infrared window channels of satellite radiometers. NOAA Tech. Rep. NESS 80, U. S. Dept. of Commerce, 40 pp.

Zehr, R. M., J. F. W. Purdom, J. F. Weaver, and R. N. Green, 1988: Use of VAS data to diagnose the mesoscale environment of convective storms. <u>Wea. and Forecasting</u>, 3, 33-49.

# ACKNOWLEDGMENTS